NATIONAL INSTITUTE FOR FUSION SCIENCE

Particle Simulation Study of Collisionless Driven Reconnection in a Sheared Magnetic Field

R. Horiuchi and T. Sato

RESEARCH REPORT
NIFS Series

NAGOYA, JAPAN

PARTICLE SIMULATION STUDY OF COLLISIONLESS DRIVEN RECONNECTION IN A SHEARED MAGNETIC FIELD

Ritoku Horiuchi and Tetsuya Sato

Theory and Computer Simulation Center,

National Institute for Fusion Science,

Nagoya 464-01, Japan

Abstract

Nonlinear development of collisionless driven reconnection and the consequent energy conversion process between the field and particles in a sheared magnetic field are investigated by means of a two-and-a-half-dimensional particle simulation. Magnetic reconnection takes place in two steps irrespective of a longitudinal magnetic field, but the growth rate of reconnection field varies in proportion to the $E \times B$ drift velocity at an input boundary. It is clearly observed that the triggering mechanism of collisionless driven reconnection for the fast growing phase changes from an electron meandering dominance in a weak longitudinal field to an electron inertia dominance in a strong field. The electron acceleration and heating take place in the reconnection area under the influence of reconnection electric field, while the electron energy is converted to the ion energy through the action of electrostatic (ambipolar) field excited by magnetic compression in the downstream. It is also found that, in the presence of a longitudinal magnetic field, the electron acceleration by the reconnection field takes place effectively and the generated force-free current is maintained for a long period while forming an asymmetric spatial profile of current layer.

I. Introduction

Driven magnetic reconnection[1] in a collisionless plasma, "collisionless driven reconnection", is an important process in considering energetically active phenomena observed in a high temperature, rarefied plasma such as solar corona,[2] geomagnetic tail,[3] fusion plasmas,[4] and so on, because it can lead to fast energy conversion from the field energy to the particle energy as well as a topological change of magnetic field in a collisionless plasma. If a current-carrying particle is lost from a current layer, an electric field is induced so as to accelerate a particle along the equilibrium current and compensate it for the momentum loss. This electric field also plays a role in changing the topology of magnetic field, i.e., magnetic field reconnection. Magnetic reconnection, however, can not take place in an ideal magnetohydrodynamic (MHD) plasma because magnetic field is frozen in a plasma. This means that non-ideal effect, which breaks the frozen-in condition and leads to the generation of electric field, is needed for the excitation of magnetic reconnection.

Because a charged particle has a finite mass and a finite temperature, it executes a complex thermal motion with a finite orbit amplitude in a spatially variable magnetic field. Therefore, the frozen-in condition of magnetic field is not applicable to microscopic scale phenomena associated with motion of charged particles even for a collisionless plasma. Collisionless reconnection has been studied by using various models based on theoretical analyses,[5–11] particle simulation,[12–17] and fluid simulation.[18,19] Two mechanisms to generate the reconnection electric field in a collisionless plasma have so far been considered in relation to such a kinetic effect. The first one is a spontaneous excitation of the electric field caused by momentum loss of current carrying particles through non-ideal effect such as wave-particle interaction[20] or collisionless tearing instability.[6–12,15,16] Another mechanism is due to the field penetration[21] when the current layer is being compressed by an external driving source. An electric field, which is induced in the MHD region outside

2

the current layer by the plasma flow moving across a magnetic field, can penetrate into the current layer through a particle kinetic effect when the current layer is compressed as thin as a characteristic length of particle kinetic effect.

In two-dimensional system there exit two types of microscale particle effect which are responsible for the decoupling of magnetic field from the particle motion in a collisionless plasma. One is the particle inertia effect which becomes significant in a spatial scale comparable to collisionless skin depth.[14,18,19] The other is the particle orbit effect which becomes effective in an excursion scale of particle thermal motion which is called a meandering motion.[10,17,22] Horiuchi and Sato[17] demonstrated two-dimensional particle simulation of collisionless driven reconnection for the case where the system is subjected to an external driving flow and there is no longitudinal magnetic field at an initial stage. They showed that magnetic reconnection is triggered by the meandering orbit effect when the current layer is compressed as thin as an excursion distance of meandering particles and that it evolves temporarily in two steps in accordance with the formation of two current layers, the widths of which are characterized by the excursion distances of the ion and electron meandering motions, respectively. Because thermal motion of a charged particle is strongly dependent on the topology of magnetic field and its strength, it is expected that collisionless driven reconnection and the resulting energy conversion process are largely affected by adding a longitudinal magnetic field.

In this paper we will give detailed discussions on the electron dynamics in a sheared magnetic field in order to clarify the difference between the electron inertia effect and the electron thermal effect on collisionless driven reconnection. For this purpose we have developed the electromagnetic (EM) particle simulation code with higher temporal and spatial resolutions compared with the former one.[17,23,24] The numerical scheme and the simulation model are described in Section 2. We reveal several new features in collisionless driven reconnection in a sheared magnetic field. For example, the triggering mechanism

3

of collisionless driven reconnection is found to change from the electron thermal effect for a weak longitudinal field to the electron inertia effect for a strong field. This phenomenon is also found to be related to the fact that an electron thermal motion becomes more strongly magnetized and its spatial scale decreases as a longitudinal field increases.

From the particle simulation we find that the ion energy increases twice as large as the electron energy through collisionless driven reconnection. The same phenomenon is observed in experimental plasmas[25] in which an MHD relaxation controlled by collisionless or collisional magnetic reconnection takes place. This phenomenon is considered to be associated with the generation of collisionless ion viscosity which leads directly to the ion heating.[26] In order to clarify this process, we examine the energy conversion process between the EM field and the charged particle through collisionless driven reconnection. Consequently, the energy conversion is found to be controlled by two important mechanisms, i.e., the electron acceleration and heating by the reconnection electric field in the vicinity of reconnection point, and the energy conversion from electron energy to ion energy through the action of an electrostatic field excited in the downstream by magnetic compression. These simulation results are discussed in detail in Section 3. Finally, a brief summary is given in Section 4.

II.   Simulation Model

Let us study externally driven magnetic reconnection of a collisionless plasma by means of two-and-one-half dimensional particle simulation. The EM simulation code which relies on the standard explicit scheme[27] is developed in order to obtain the nonlinear evolution of an open system. Because both electrons and ions are treated as particles in this method, a finite electron Larmor radius effect can be described as well as a finite ion Larmor radius effect. The physical quantities are assumed to be translationally symmetric in the

4

z-direction ($\partial/\partial z = 0$). The basic equations to be solved are the equations of motion

$$\frac{d(\gamma_j \mathbf{v}_j)}{dt} = \frac{q_j}{m_j} [\mathbf{E} + \frac{\mathbf{v}_j}{c} \times \mathbf{B}], \tag{1}$$

$$\frac{d\mathbf{x}_j}{dt} = \mathbf{v}_j, \tag{2}$$

and the Maxwell equations

$$\frac{1}{c}\frac{\partial A_z}{\partial t} = -E_z, \tag{3}$$

$$\frac{1}{c}\frac{\partial B_z}{\partial t} = -\frac{\partial E_y}{\partial x} + \frac{\partial E_x}{\partial y}, \tag{4}$$

$$\frac{1}{c}\frac{\partial \mathbf{E}}{\partial t} = \nabla \times \mathbf{B} - 4\pi\mathbf{j}, \tag{5}$$

$$\nabla \cdot \mathbf{E} = 4\pi\rho, \tag{6}$$

where

$$B_x = \partial A_z/\partial y, \quad B_y = -\partial A_z/\partial x, \tag{7}$$

A_z, $\mathbf{x}_j(t)$, $\mathbf{v}_j(t)$, m_j and q_j are the z-component of the vector potential, the position, the velocity, the rest mass and the charge of the j-th particle, and the relativistic γ-factor of the j-th particle is defined by

$$\gamma_j = 1/\sqrt{1 - (\mathbf{v}_j \cdot \mathbf{v}_j)/c^2}. \tag{8}$$

The current density $\mathbf{j}(\mathbf{x}, \mathbf{t})$ and the charge density $\rho(\mathbf{x}, t)$ are obtained by summing over all the particles, namely,

$$\mathbf{j}(\mathbf{x}, \mathbf{t}) = \sum_{j=1}^{N} \frac{q_j \mathbf{v}_j(t)}{c} S(\mathbf{x} - \mathbf{x}_j(t)), \tag{9}$$

$$\rho(\mathbf{x}, t) = \sum_{j=1}^{N} q_j S(\mathbf{x} - \mathbf{x}_j(t)), \tag{10}$$

where N is the total number of particles and $S(\mathbf{x})$ is the form function of particles.[17,27]

As an initial condition we adopt a one-dimensional equilibrium with a sheared magnetic field as

$$\mathbf{B}(y) = (B_x(y), 0, B_{z0}), \tag{11}$$

5

$$B_x(y) = B_0 \tanh(y/L), \tag{12}$$

$$P(y) = B_0^2/8\pi \; \mathrm{sech}^2(y/L), \tag{13}$$

where B_{z0} is a constant and L is the scale height along the y-axis. There is a magnetically neutral sheet along the mid-horizontal line ($y = 0$) in the initial equilibrium for the case of $B_{z0} = 0$. The vector potential A_z is set zero along the mid-horizontal line at $t = 0$. Let us assume that the initial particle distribution is given by a shifted Maxwellian with a spatially constant temperature and the average particle velocity is equal to the diamagnetic drift velocity. Then, the particle position and the particle velocity are determined from the pressure profile $P(y)$ and the current density $\mathbf{j}(\mathbf{x}, 0)$ ($ = (0, 0, -B_0/(4\pi L) \; \mathrm{sech}^2(y/L))$). Because both an ion and an electron are loaded at the same spatial position, there is no electric field in the initial profile.

In order to drive magnetic reconnection at the center of the simulation domain we adopt an input boundary condition[17,24] at the boundary of the y-axis ($y = \pm y_b$) and a periodic boundary condition at the boundary of the x-axis ($x = \pm x_b$). At the input boundary the y-derivatives of the magnetic field quantities are equal to zero and the plasma is smoothly supplied with the $\mathbf{E} \times \mathbf{B}$ drift velocity into the simulation domain. The driving electric field is determined so as to be always normal to both the magnetic field and the input flow velocity. The amplitude of driving electric field $E_{d0}(x, t)$ is taken to be zero at $t = 0$ and gradually increases for $0 < \omega_{pe}t < 100$ (ω_{pe} is an average electron plasma frequency). After this period ($\omega_{pe}t > 100$), $E_{d0}(x, t)$ is described by a symmetric constant profile with a maximum input rate of magnetic flux E_0 at the center of the input boundary.

We have extended the semi-implicit EM code to the explicit EM simulation code which can resolve an electron kinetic effect with a high accuracy. One million and six hundred thousand particles are used for the present simulation. The ratio of the side lengths of the simulation box x_b/y_b is fixed to 3. The simulation domain is implemented on a (256×128)

point grid. The time step width Δt is determined so as to satisfy the Courant-Friedrichs-Lewy condition[28] for the electromagnetic wave in vacuum; the relation $\Delta t = 0.5\Delta y/c$ holds in our simulation where Δy ($= 0.7\lambda_D$) is the grid separation along the y-axis and λ_D is the Debye length associated with an average number density at $t = 0$.

III. Simulation Results

We carry out six simulation runs with different values of an initial longitudinal magnetic field B_{z0}. The simulation starts from the equilibrium profile the scale height of which is comparable to the ion Larmor radius ρ_{xi} associated with the asymptotic in-plane field B_0, i.e., $L \approx 51\Delta y$, $\rho_{xi} \approx 25\Delta y$. Other typical parameters are as follows: the ratio of ion to electron mass M_i/M_e is 25, the maximum value of driving electric field E_0 is $-0.04B_0$, $\omega_{pe}/\omega_{ce} = 5.0$, $c/(\omega_{pe}\Delta y) \approx 12$, and $\omega_{ce}\Delta t \approx 0.01$, where ω_{ce} ($= eB_0/M_e c$) is the electron cyclotron frequency. The relation $L > \rho_{xi} > c/\omega_{pe} > \Delta y$ holds in the initial profile for all cases.

A. Fundamental properties of collisionless driven reconnection

In this sub-section we examine the fundamental properties of collisionless driven reconnection by comparing the simulation results for the case of $B_{z0} = 0$ with those obtained from the semi-implicit particle simulation.[17] Figure 1 shows the contour plots of the current density $-j_z$ (top), those of the vector potential A_z (second), the vector plots of the average ion velocity (third), and those of the average electron velocity (bottom) in the (x,y) plane at $\omega_{ce}t = 100$ where the current density contours less than the average value and the vector potential contours less than the initial value at the input boundary are plotted by dotted lines. The current density profile becomes peaked at the midpoint of

the simulation domain because the plasma flow supplied through the boundary has a maximum input velocity at the midpoint of the input boundary ($x = 0, y = \pm y_b$). An x-shaped structure of magnetic separatrix becomes visible as a result of magnetic reconnection. A fast directed flow arises from the x-point after magnetic reconnection sets in and carries the reconnected flux toward the boundaries of the x-axis. The current density profile becomes elongated along the x-axis by the divergent plasma flow and its spatial scale reaches about a half of the x-side length of the simulation box. It is interesting to note that a clear x-shaped shock structure appears in the electron flow pattern while the ion flow pattern looks relatively faint due to the finite ion Larmor radius effect. The maximum value of the electron average velocity is about three times as large as that of the ion average velocity. This means that the in-plane components of electric current appear in the downstream as a result of magnetic reconnection.

Figure 2 shows (a) the temporal evolution of the reconnection electric field $E_z^{(1)}$, (b) the temporal evolutions of four spatial scales and (c) those of the electron number density (solid line) and the ion number density (dotted line) at the reconnection point where d_{Bx}, $d_{skin} = c/\omega_{pe}$, l_{mi} and l_{me} in Fig. 2-(b) are the scale height of magnetic field B_x along y-axis, the electron skin depth associated with the electron number density inside the current layer, the average orbit amplitude of meandering ions and that of meandering electrons, respectively. The average amplitude of meandering motion is estimated by the particle temperature and the longitudinal magnetic field B_z averaged over the current layer and the in-plane magnetic field B_x just outside the current layer. It is clear from Fig. 2 that there are two temporal phases in the evolution of the reconnection field, i.e., the slow reconnection phase for $0 < \omega_{ce}t < 80$ and the fast reconnection phase for $80 < \omega_{ce}t < 100$. The growth rate is estimated to be $\gamma_1 \approx 0.03\omega_{ce}$ for the slow reconnection phase and $\gamma_2 \approx 0.07\omega_{ce}$ for the fast reconnection phase. These values are a few times as large as those of the semi-implicit study. This difference may come from the fact that the width of

8

the initial current layer d_{Bx} is comparable to the excursion length of a meandering ion l_{mi} for the present case while the width is about two times as large as the ion excursion length for the former case. In other words, this suggests that the growth rate of the reconnection field strongly depends on the width of the current layer. The fact that the scale height d_{Bx} is comparable to l_{mi} in the first half of the slow reconnection phase means that a finite ion Larmor radius effect becomes active in the current layer even at the starting period of the simulation. This is deeply connected with the phenomenon that the reconnection field grows slowly as soon as the simulation starts. The number densities at the center of the current layer increase due to the compression by the convergent plasma flow as time goes on, while the scale height d_{Bx} decreases and the current layer becomes narrower and narrower.

The width of the current layer approaches the average orbit amplitude of meandering electrons at the end of the slow reconnection phase. The fast reconnection phase starts after the number densities reaches the maximum value at $\omega_{ce}t \approx 70$. It is observable in Fig. 2(c) that the electron density becomes slightly dominant over the the ion number density in the fast phase. The violation of charge neutrality condition leads to the fast growth of an electrostatic field in the current layer (electron current layer). This is because an electron motion is more strongly restricted by the motion of magnetic field compared with an ion motion due to the finite Larmor radius effect. These results are consistent with the results obtained from the semi-implicit particle study. It is worthy to note that the width of electron current layer in the fast reconnection phase is determined by the excursion distance of electron meandering motion but not by the electron skin depth, i.e., the fast reconnection is triggered mainly by the electron meandering (thermal) effect but not by the electron skin depth (inertia) effect for this case.

9

B.   Energy conversion by electric field

The reconnection electric field leads to not only the topological change of magnetic field lines but also the energy conversion from the field energy to the particle energy through the acceleration and heating processes. Figure 3 shows (a) the temporal evolution of the average ion energy, (b) that of the average electron energy for the case of $B_{z0} = 0$, (c) that of the average ion energy, (d) that of the average electron energy for the case of $B_{z0} = 2B_0$, where the solid, dotted, and dashed lines stand for the x-component, the y-component, and the z-component of the energy per a particle averaged over the whole domain, respectively. The z-component is larger than the other components by the energy of a diamagnetic motion at $t = 0$.

Only the y-component of the ion energy increases in the initial compression phase because the y-component of the ion kinetic energy is dominant in the plasma flow supplied through the input boundary. This energy is transferred to the z-component in a quarter of an ion gyration period ($\approx 40\omega_{ce}^{-1}$) because an ion gyrates in the (y,z) plane for $B_{z0} = 0$. On the other hand, for the case of $B_{z0} = 2B_0$, the ion energy of the input flow is transferred to the x-component predominantly because an ion gyrates almost in the (x,y) plane due to the strong B_z field.

For the case of $B_{z0} = 0$, both the x-component of the ion energy and that of the electron energy increase rapidly after the reconnection electric field becomes maximum ($t = 100\omega_{ce}^{-1}$). The time used for the energy conversion from the field energy to the ion energy is relatively longer compared with that to the electron energy and the saturation value of the ion energy becomes two times as large as that of the electron energy. The energy conversion occurs more actively in the plasma without any longitudinal magnetic field. These differences come from the nature of the energy conversion mechanism in the presence of the electric field, as will be discussed in the followings.

10

Because the temporal change of the total field energy is described by

$$\frac{d}{dt} \int d^3x \{\frac{\mathbf{B}^2}{8\pi} + \frac{\mathbf{E}^2}{8\pi}\} = \int d^3x \{\nabla \cdot (\frac{\mathbf{B} \times \mathbf{E}}{4\pi}) - \mathbf{E} \cdot \mathbf{j}\}, \tag{14}$$

the energy conversion between the field and the particles in the plasma is carried out through the work done by the electric field, i.e., the term $\mathbf{E} \cdot \mathbf{j}$. In order to obtain the detailed information of this conversion process, let us decompose the electric field and the electric current as

$$\mathbf{E} = \mathbf{E}_{st} + \mathbf{E}_{mg}, \tag{15}$$

$$\mathbf{j} = \mathbf{j}_i + \mathbf{j}_e, \tag{16}$$

where $\mathbf{E}_{st}$, $\mathbf{E}_{mg}$, $\mathbf{j}_i$, and $\mathbf{j}_e$ are the electrostatic component, the electromagnetic component, the ion current, and the electron current, respectively. Figure 4 shows the color-coded contour maps of the energy conversion rates $\mathbf{E}_{mg} \cdot \mathbf{j}_i$ (top), $\mathbf{E}_{st} \cdot \mathbf{j}_i$ (second), $\mathbf{E}_{mg} \cdot \mathbf{j}_e$ (third), and $\mathbf{E}_{st} \cdot \mathbf{j}_e$ (bottom) in the (x,y) plane for the case of $B_{z0} = 0$ where $\mathbf{E}_{mg} \cdot \mathbf{j}_i$, $\mathbf{E}_{st} \cdot \mathbf{j}_i$, $\mathbf{E}_{mg} \cdot \mathbf{j}_e$, and $\mathbf{E}_{st} \cdot \mathbf{j}_e$ stand for the energy conversion rate to the ion energy by the electromagnetic component, that to the ion energy by the electrostatic component, that to the electron energy by the electromagnetic component, that to the electron energy by the electrostatic component, respectively. The red and blue colors in Fig. 4 stand for the positive and negative rates, respectively. For example, the bottom panel shows that the energy is converted from the particle to the field. There are two spatial regions in which the energy conversion occurs actively, i.e., the vicinity of the reconnection point and the shock-like region in the downstream. The electromagnetic component $\mathbf{E}_{mg}$, which is dominated by the reconnection field E_z, acts on the particles in the vicinity of the reconnection point and leads mainly to the increase of the electron energy.

On the other hand, the electrostatic field $\mathbf{E}_{st}$, which has only the x- and y-components, becomes significant at the shock-like region in the downstream, and leads to the rapid increase of the ion energy and the decrease of the electron energy. The mechanism is as

11

follows. Magnetic reconnection leads to the topological change of magnetic field as well as the electron acceleration along the z axis in the vicinity of the reconnection point. In other words, both the transverse component of magnetic field B_y and the strong electron current j_z are generated as a result of magnetic reconnection. When an electron moves outside the narrow reconnection area, it becomes magnetized to be accelerated along the x axis by the resultant $j \times B$ force. The electron acceleration becomes so strong that the average electron velocity in the downstream is much larger than the average ion velocity (see Fig. 1) and the net electric current along the x axis appears in the downstream. The mass density profile is dynamically compressed by the magnetic flux which is carried by the divergent plasma flow. The electrostatic field is strongly generated in the region with steep density gradient due to the finite Larmor radius effect. This electrostatic field, in turn, works on decelerating the electron flow and accelerating the ion flow in the downstream, that is to say, the ambipolar interaction by the electrostatic field leads to the fast energy conversion from the electron energy to the ion energy in the downstream. It is important to note that, in the vicinity of the reconnection point, the energy conversion rate by the electrostatic field is negligibly small compared with that by the electromagnetic component. In other words, the electrostatic field plays a leading role on neither the particle acceleration nor the thermalization in the vicinity of the reconnection point.

The temporal evolutions of the total conversion rates are shown in Fig. 5-(a) for the case of $B_{z0} = 0.0$ where the total rate is obtained by integrating over the whole simulation area. The total conversion rates to the ion energy by the electromagnetic and electrostatic components are always positive ($\mathbf{E}_{st} \cdot \mathbf{j}_i, \mathbf{E}_{mg} \cdot \mathbf{j}_i > 0$). That is, the energy is monotonously converted from the electromagnetic field to the ions. On the other hand, the electrons get the energy through the action of reconnection field ($\mathbf{E}_{mg} \cdot \mathbf{j}_e > 0$) and lose it under the influence of the electrostatic field in the downstream ($\mathbf{E}_{st} \cdot \mathbf{j}_e < 0$). These facts explain why the ion energy increases twice as large as the electron energy

12

(see Fig. 3). Furthermore, we can find an interesting feature in Fig. 5-(a) that two conversion rates by the electrostatic field, $\mathbf{E}_{st} \cdot \mathbf{j}_i$ (dotted curve) and $\mathbf{E}_{st} \cdot \mathbf{j}_e$ (solid curve), reveal the very similar behavior to each other except the fact that the ion rate is always positive and the electron rate always negative. This result means that the electrostatic (ambipolar) field excited in the downstream acts as an energy conversion channel from the electrons to the ions in a collisionless plasma. The dependence of total conversion rates from the field energy to the electron energy on the longitudinal field B_{z0} is shown in Fig. 5-(b). The conversion rate by the electromagnetic component $\mathbf{E}_{mg} \cdot \mathbf{j}_e$ becomes smaller as B_{z0} increases, but it is always positive for any cases. On the other hand, the rate by the electrostatic component $\mathbf{E}_{st} \cdot \mathbf{j}_e$ is always negative irrespective of the values of B_{z0}. These results imply that, on a whole, the electromagnetic component or the reconnection electric field acts always on increasing the electron energy, while the electrostatic component works always on decreasing the electron energy, irrespective of the existence of a longitudinal magnetic field.

C.   Particle acceleration and heating

In this subsection we examine the energy conversion process along the particle trajectory for the case of $B_{z0} = 0$. For this purpose we mark about six thousands electrons and ions which exist in the vicinity of the reconnection point at $\omega_{ce}t = 100$ when the reconnection electric field reaches its maximum value. Distribution function of marked electrons is given in Fig. 6 as a function of v_z where the top, middle and bottom panels represent the distribution functions at $\omega_{ce}t = 82$, 100, and 118, respectively. We can observe that the electron distribution shifts towards the positive v_z direction as a whole while making its profile broader when the electrons pass across the reconnection area ($\omega_{ce}t = 100$). That is, the electron heating and acceleration along the z-axis take place simultaneously. Most of the electron average momentum along the z-axis is lost and the distribution becomes

further broader at $\omega_{ce}t = 118$ when the electrons move in the downstream.

Let us examine the particle heating and acceleration process in more detail. Figure 7 shows (a) the temporal evolutions of the average velocity, the thermal velocity, and the average vector potential A_z of the marked electrons, (b) those of the marked ions, and (c) the temporal evolutions of four energy-conversion rates evaluated at particle positions, $-\mathbf{E}_{st} \cdot \mathbf{u}_e$, $-\mathbf{E}_{mg} \cdot \mathbf{u}_e$, $\mathbf{E}_{st} \cdot \mathbf{u}_i$, and $\mathbf{E}_{mg} \cdot \mathbf{u}_i$. The spatial position of marked particles is expressed in terms of the normalized vector potential which is unit at the input boundary, zero at the reconnection point, and negative in the downstream. The x and y components of the average particle velocity in Figs. 7(a) and 7(b), u_x and u_y, are illustrated so as to be negative for the convergent flow and positive for the divergent flow.

The electron acceleration and thermalization along the z-direction take place rapidly as soon as they enter into the reconnection area, as was seen in Fig. 6. The time scale of electron acceleration and thermalization is estimated to be about $10/\omega_{ce}$ which is in good agreement with the time τ_e needed for a thermal electron to pass through the electron current layer, i.e. $\tau_e = 2l_{me}/v_{te}$. This agreement also implies that both the electron acceleration and thermalization processes become active when the electrons exist in the reconnection area defined by the width of the electron current layer. The reconnection area corresponds to the diffusion area in the fluid model. The behavior of u_x in Fig. 7(a) exhibits that the electron flow is changed from the convergent type ($u_x < 0$) to the divergent type ($u_x > 0$) when they pass across the reconnection point ($A_z = 0$). The transverse (y) component of magnetic field is created as a result of magnetic reconnection. The fast electron motion toward the downstream sides along the x-axis is generated mainly by the resultant $\mathbf{j}_e \times \mathbf{B}$ force. The electron motion is gradually decelerated by the electrostatic field in the downstream as the electrons move from the vicinity of the reconnection point to the downstream sides. Thus, the average electron velocity vanishes in the downstream. In contrast to this, the electron thermal velocity

14

remains almost constant in the downstream.

Because unmagnetized region for ions is wider and ion thermal velocity is lower compared with those for electrons, thermal ions remain in the reconnection area for a relatively long period. The time τ_i needed for a thermal ion to pass through the reconnection area is estimated to be about $30/\omega_{ce}$. As $\tau_i >> \tau_e$, the ions are accelerated along the z-axis for a relatively long period by the reconnection electric field when they pass across the vicinity of the reconnection point. The z-component of the ion average velocity becomes about 2.0 of the initial Alfven velocity v_{A0} when the ions go outside the reconnection area. On the other hand, there is no significant change in the thermal velocity when the ions pass through the reconnection area. One can find that the ions are thermalized more effectively by the electrostatic field rather when they move in the downstream ($t > 130\omega_{ce}$) than when they exist inside the reconnection area ($t < 130\omega_{ce}$). Thus, it is concluded that the electron heating takes place in the reconnection area under the influence of reconnection electric field while the ion heating takes place in the downstream by the action of electrostatic field.

D. Reconnection mechanism

It has so far been pointed out that there exist two mechanisms associated with microscale particle effect which lead to magnetic reconnection in a collisionless plasma. One is a particle inertia effect which becomes significant in a spatial scale comparable to collisionless skin depth c/ω_p. The other is a particle orbit effect which becomes effective in an excursion distance of particle meandering motion. We have observed that magnetic reconnection is controlled by a meandering orbit effect for the case of $B_{z0} = 0$ where an excursion distance of a meandering electron is larger than an electron skin depth in the current layer. The excursion distance of meandering motion in the current layer becomes shorter and so a charged particle becomes more strongly magnetized as a longitudinal

15

magnetic field becomes stronger, as is shown in Fig. 8. Because collisionless driven reconnection is deeply connected with meandering motion of charged particles in the current layer, it is natural to expect that both the magnetic reconnection and energy conversion processes are largely affected by a longitudinal magnetic field.

First, let us examine the influence of a longitudinal field on the behavior of reconnection electric field. The temporal evolution of the reconnection electric field is shown in Fig. 9 for five different values of B_{z0}. Careful examination of Fig. 9 reveals that there exist both the slow reconnection phase and the fast reconnection phase irrespective of a longitudinal field. However, both the growth rate and the saturation value of reconnection electric field decrease as a longitudinal field becomes stronger. The growth rate for the slow phase γ_1 and that for the fast phase γ_2 are shown in Fig. 10 as a function of B_{z0}/B_0 where the maximum $\mathbf{E} \times \mathbf{B}$ drift velocity at the input boundary, $v_{in} = v_{n0}/\{1 + (B_{z0}/B_0)^2\}^{1/2}$ (v_{n0} is constant), is added for comparison. One can find that both the growth rates γ_1 and γ_2 reveal the very similar behavior to the input plasma velocity v_{in}. Because the maximum input rate of the in-plane magnetic flux is approximately given by $E_0/\{1 + (B_{z0}/B_0)^2\}^{1/2}$, this results implies that the growth of reconnection electric field is controlled by the input rate of the in-plane magnetic flux at the boundary. In other words, the whole dynamical behavior of collisionless driven reconnection is determined by the external condition such as a flux input rate into the system even if magnetic reconnection would be triggered by microscale electron mechanism in the central region of current layer. In this sense, this result is also in good agreement with the result of the semi-implicit study.[17]

Now let us turn to the triggering mechanism of collisionless driven reconnection in the fast phase. In this phase the current layer is compressed so thin that a microscale electron effect becomes visible and magnetic flux inside the current layer is no longer frozen in the electron fluid. Figure 11 illustrates the dependence of four spatial scales on the field ratio B_{z0}/B_0 when the current layer becomes thinnest in the fast reconnection

phase. The width is nearly equal to the average orbit amplitude of meandering electrons l_{me} and is two times as large as the electron skin depth c/ω_{pe} for the case of $B_{z0} = 0$ (see also Fig. 2-(b)). The excursion distance l_{me} decreases as a longitudinal field increases. This corresponds to the fact that unmagnetized region for electrons becomes narrower with a longitudinal field, as was seen in Fig. 8. On the other hand, the electron skin depth increases slightly with B_{z0}/B_0 because the plasma becomes less compressible and the increase of plasma density in the current layer is suppressed by a longitudinal field for $B_{z0} \gg B_0$. Thus, the relation $l_{me} < c/\omega_{pe}$ holds for a strong longitudinal field of $B_{z0} > 1.5B_0$. In other words, the electron inertia scale is longer than the electron thermal scale for $B_{z0} > 1.5B_0$. It is clearly seen in Fig. 11 that the width of current layer decreases with the electron thermal scale l_{me} until l_{me} reaches c/ω_{pe}. When $l_{me} < c/\omega_{pe}$, the width ceases to decease and exhibits the same behavior with the electron skin depth. Namely, collisionless driven reconnection in the fast reconnection phase proceeds keeping the width of current layer nearly equal to the electron skin depth for a strong longitudinal field of $B_{z0} > 1.5B_0$. These results lead us to the conclusion that the triggering mechanism for collisionless driven reconnection in the fast reconnection phase changes from the electron thermal effect to the electron inertia effect in accordance with the increase of a longitudinal magnetic field.

E. Asymmetric current profile

A longitudinal field has an influence on the physical processes responsible for collisionless driven reconnection, i.e., the plasma compressibility, the magnetization of a charged particle, the reconnection rate, and so on. In this subsection we present another phenomenon which appears under the influence of a longitudinal field. The reconnection electric filed accelerates the charged particles in the direction normal to the reconnection magnetic field, i.e., in the z-direction. If the z-component of magnetic field is nonzero, the

acceleration by the reconnection field creates the electric current parallel to the magnetic field. Let us consider the influence of the parallel electric current on the collisionless reconnection process. Figure 12 shows the spatial profiles of the current density along the z-axis (top) and in the (x,y) plane (bottom) at $\omega_{ce}t = 118$ for the case of $B_{z0} = B_0$. Comparing Fig. 12 with Fig. 1 one can find that the spatial structure of current layer becomes longer and asymmetric by adding a longitudinal magnetic field.

Let us consider the mechanism leading to the asymmetric current profile. For the case of $B_{z0} = 0$, the straight elongated current layer is formed as a result of magnetic reconnection, as was seen in Fig. 1. A fast divergent electron flow along the x-axis in the current layer carries the net electric current because the average electron velocity is about three times as large as the average ion velocity. The resultant $\mathbf{j} \times \mathbf{B}$ force, in turn, acts on the electron in the negative z-direction ($j_x B_y < 0$) while the average electron motion carrying the equilibrium current directs to the positive z-direction ($u_{ez} > 0$). Consequently, the average electron velocity along the z-axis is gradually lost as the fast electron flow moves towards the downstream. In this process there exists no force which modifies the current layer in an asymmetric form. Thus, the elongated current layer is terminated in the downstream and its shape is maintained symmetric with respect to the mid-horizontal line for the case of $B_{z0} = 0$.

Suppose that a longitudinal magnetic field of $B_{z0} >> B_0$ is superposed on this symmetric profile. The $\mathbf{j} \times \mathbf{B}$ force associated with the longitudinal field and the electron current along the x-axis is in the negative y-direction for the left half of the simulation plane ($x < 0$) and in the positive y-direction for the right half of the simulation plane ($x > 0$). When the electron reaches the half way of the current layer along the x-axis, the effect of the $\mathbf{j} \times \mathbf{B}$ force is visible in the electron current profile. The bending of the current layer proceeds so that the electron current becomes parallel to the the magnetic field, i.e. the force-free condition is satisfied between the electric current and the magnetic field.

18

Therefore, the parallel current enhanced by the reconnection field is maintained for a long period when the fast plasma flow moves in the bent current layer at the downstream.

We have another evidence that the force-free current is maintained for a long period in the downstream in the presence of the longitudinal field. Figure 13 shows the temporal evolutions of the average velocity along the z-axis for about six thousands marked electrons which pass across the vicinity of the reconnection point when the reconnection electric field reaches its maximum value. The electrons are accelerated by the reconnection electric field when they exist in the reconnection area. The force-free current generated through the acceleration by the reconnection field is maintained for a long period in the downstream in the presence of the longitudinal field, while, for the case of $B_{z0} = 0$, the average electron momentum is immediately lost as soon as they moves into the downstream. It is interesting to note that the maximum electron velocity increases with B_{z0} although the reconnection field decreases as B_{z0} increases (see Fig. 9). This implies that the existence of a longitudinal magnetic field makes it easy for the reconnection field to accelerate the electrons along the z-axis. This phenomenon is also expressed in terms of effective resistivity η_{eff} which is given by the ratio of the electric field to the current density at the reconnection point, i.e., E_z/j_z. The temporal evolution of the effective resistivity is illustrated in Fig. 14 for five different values of B_{z0} where the resistivity is normalized by the Hall resistivity B_0/qcn_e. Figure 14 clearly shows that the effective resistivity varies inversely with B_{z0}. This means that the electric field needed for maintaining the electric current decreases as a longitudinal field increases. It is concluded that, under the influence of a longitudinal magnetic field, the electron acceleration by the reconnection field takes place effectively and the generated force-free current is maintained for a long period while forming an asymmetric spatial profile of current layer.

19

IV.   Summary

We have investigated the nonlinear development of collisionless driven reconnection and the consequent energy conversion between particles and an electromagnetic field in a sheared magnetic field by making use of a two-and-one-half dimensional particle simulation. The main results are summarized by following six remarks.

(A) The reconnection electric field evolves in two steps irrespective of an existence of longitudinal magnetic field, i. e., 1) slow reconnection triggered by ion kinetic effect in the early phase, and 2) fast reconnection triggered by electron kinetic effect in the late phase. The existence of these two temporal phases is deeply connected with the formation of two types of current layer, i. e., electron current layer and ion current layer.

(B) The growth rate of reconnection electric field and its saturation value are determined by the flux input rate at the boundary, but not by the detailed mechanism leading to collisionless reconnection in the current layer. This is an important feature which is commonly observed in the phenomena triggered by driven magnetic reconnection.[1]

(C) There are two microscopic particle effects which lead to collisionless magnetic reconnection in a two-dimensional system. For a weak longitudinal magnetic field case, the width of electron current layer is determined by the excursion distance of electron meandering motion. As the longitudinal magnetic field increases, thermal motion becomes more strongly magnetized and the excursion distance of meandering electrons becomes shorter. For a strong longitudinal field case where the electron skin depth is larger than the excursion distance of meandering electron motion, the inertia effect becomes dominant and the width of electron current layer is determined by the electron skin depth.

(D) The electron acceleration and thermalization take place in the reconnection area under the influence of reconnection electric field. On the other hand, the electrostatic field plays a leading role on neither the particle acceleration nor the thermalization in the vicinity of the reconnection point.

(E) The electrostatic field, which is generated in the downstream as a result of magnetic compression by the divergent reconnection flow, acts as an energy conversion channel from the electrons to the ions in a collisionless plasma. Thus, the total ion energy becomes twice as large as the total electron energy. The energy conversion takes place more actively in the plasma without any longitudinal magnetic field and its rate decreases with a longitudinal field.

(F) The existence of a longitudinal magnetic field makes it easy for the electric field to accelerate electrons along the equilibrium current at the reconnection point and plays a role in maintaining the generated force-free current for a long period by forming an asymmetric spatial profile of current layer.

The present particle simulation study has clarified the particle kinetic effect in collisionless driven reconnection, based on two-dimensional model in which the spatial dependence along the equilibrium current has been ignored The interaction between particles carrying electric current and a wave propagating along the electric current becomes an origin of an anomalous resistivity[20] which can also lead to collisionless reconnection. Three-dimensional treatment is needed for the investigation of this effect in collisionless driven reconnection and the relation between the particle kinetic effect and the effect of wave-particle interaction.

Acknowledgments

References

1. T. Sato and T. Hayashi, Phys. Fluids **22**, 1189(1979); T. Sato, T. Hayashi, K. Watanabe, R. Horiuchi, M. Tanaka, N. Sawairi and K. Kusano, Phys. Fluids B **4**, 450(1992).

2. E. R. Priest, *Solar Magnetohydrodynamics* (Dordrecht,Reidel,1982).

3. A. Nishida, *Geomagnetic Diagnostics of the Magnetoshpere* (Springer-Verlang, New York, 1978).

4. T. Sato, Y. Nakayama, T. Hayashi, K. Watanabe, and R. Horiuchi, Phys. Rev. Lett. **63**, 528(1989); M. Yamada, Y. Ono, A. Hayakawa, M. Katsurai, and F. W. Perkins, Phys. Rev. Lett. **65**, 721(1990); R. Horiuchi and T. Sato, Phys. Fluids B **4**, 672(1992).

5. W. Horton and T. Tajima, Geophys. Res. Lett. **17**, 123(1990).

6. G. Laval, R. Pellat, and M. Vuillemin, *Plasma Physics and Controlled Fusion Research* (International Atomic Energy Agency, Vienna, 1966), Vol. II, p. 259.

7. B. Coppi, G. Laval, and R. Pellat, Phys. Rev. Lett. **16**, 1207(1966).

8. K. Schinder, J. Geophys. Res. **79**, 2803(1974).

9. J. D. Drake and Y. C. Lee, Phys. Rev. Lett. **39**, 453(1977).

10. A. A. Galeev, *Basic Plasma Physics II* (North-Holland Physics Publishing, New York, 1984), p.305.

11. X. Wang and A. Bhattacharjee, J. Geophys. Res. **98**, 19419(1993).

12. I. Katanuma and T. Kamimura, Phys. Fluids **23**, 2500(1980).

13. J. N. Leboeuf, T. Tajima and J. M. Dawson, Phys. Fluids **25**, 784(1982).

14. D. W. Hewett, G. E. Frances and C. E. Max, Phys. Rev. Lett. **61**, 893(1988).

15. W. Zwingmann, J.Wallance, K. Schindler, and J. Birn, J. Geophys. Res. **95**, 20877(1990).

16. P. L. Pritchett, F. V. Coroniti, R. Pellat, and H. Karimabadi, J. Geophys. Res. **96**, 11523(1991).

17. R. Horiuchi and T. Sato, Phys. Plasmas **1**, 3587(1994).

18. M. Ottaviani and F. Forcelli, Phys. Rev. Lett. **71**, 3802(1993).

19. D. Biskamp, E. Schwarz, and J. F. Drake, Phys. Rev. Lett. **75**, 3850(1995);B. Rogers and L. Zakharov, Phys. Plasmas **3**, 2411 (1996).

20. For example, R. C. Davidson and N. T. Gladd, Phys. Fluids **18**, 1327(1975); P. C. Liewer and R. C. Davidson, Nucl. Fusion **17**, 85(1977); A. A. Galeev and R. Z. Sagdeev, *Basic Plasma Physics II* (North-Holland Physics Publishing, New York, 1984), p.271; M. Tanaka and T. Sato, J. Geophys. Res. **86**, 5541(1981).

21. A. Fruchtman and K. Gomberoff, Phys. Fluids B **5**, 2371(1993).

22. R. Horiuchi and T. Sato, Phys. Fluids B **2**, 2652(1990).

23. M. Tanaka and T. Sato, Phys. Fluids **29**, 3823(1986).

24. S. Murakami and T. Sato, J. Phys. Soc. Japan **61**, 849(1992).

25. T. Fujita, K. Saito, J. Matsui, Y. Kamada, H. Morimoto, Z. Yoshida, and N. Inoue, Nucl. Fusion **31**, 3(1991).

26. Z. Yoshida and A. Hasegawa, Phys. Fluids **B4**, 3013(1992).

27. C. K. Birdsall and A. B. Langdon, *Plasma Physics via Computer Simulation* (McGraw-Hill, New York, 1985).

28. R. Courant, K. O. Friedrichs, and H. Lewy, Math. Ann. **100**, 32(1928).

Fig. 1.   Contour plots of the current density $-j_z$ (top), those of the vector potential A_z (second), the vector plots of the average ion velocity (third), and those of the average electron velocity (bottom) in the (x,y) plane at $\omega_{ce}t = 100$ for the case of $B_{z0} = 0$ where the current density contours less than the average value and the vector potential contours less than the initial value at the input boundary are plotted by dotted lines.

Fig. 2.   Temporal evolutions of (a) the reconnection electric field $E_z^{(1)}$, (b) four spatial scales and (c) the electron number density (solid line) and the ion number density (dotted line) at the reconnection point for the same case as Fig. 1. Here d_{Bx}, $d_{skin} = c/\omega_{pe}$, l_{mi} and l_{me} in Fig. 2-(b) are the scale height of magnetic field B_x, the electron skin depth, the average orbit amplitude of meandering ions and that of meandering electrons, respectively.

Fig. 3.   Temporal evolutions of (a) the average ion energy for $B_{z0} = 0$, (b) the average electron energy for $B_{z0} = 0$, (c) the average ion energy for $B_{z0} = 2B_0$, and (d) the average electron energy for $B_{z0} = 2B_0$ where the solid, dotted, and dashed lines stand for the x-component, the y-component, and the z-component of the energy per a particle averaged over the whole domain, respectively.

Fig. 4.   The color-coded contour maps of the energy conversion rates $\mathbf{E}_{mg} \cdot \mathbf{j}_i$ (top), $\mathbf{E}_{st} \cdot \mathbf{j}_i$ (second), $\mathbf{E}_{mg} \cdot \mathbf{j}_e$ (third), and $\mathbf{E}_{st} \cdot \mathbf{j}_e$ (bottom) in the (x,y) plane for the same case as Fig. 1 where the red and blue colors stand for the positive and negative rates, respectively.

Fig. 5.   Temporal evolutions of (a) four components of the total energy conversion rate between the field and particles for $B_{z0} = 0.0$, and (b) the total conversion rates from the field to the electrons for four different longitudinal fields.

Fig. 6. Distribution functions of about six thousands marked electrons at $\omega_{ce}t = 82$ (top), 100 (middle), and 118 (bottom) for the same case as Fig. 1.

Fig. 7. Temporal evolutions of (a) the average velocity, the thermal velocity, and the average vector potential A_z of the marked electrons, (b) those of the marked ions, and (c) four energy conversion rates evaluated at particle positions for the same case as Fig. 1.

Fig. 8. Excursion distance of a test particle in a one-dimensional sheared magnetic field where l_m, l_{mx}, ρ_x, and ρ_z are an average excursion distance in a sheared field, that for $B_{z0} = 0.0$, the Larmor radius associated with an in-plane field B_0, and that associated with a longitudinal field B_{z0}, respectively.

Fig. 9. Temporal evolution of the reconnection electric field for five different values of B_{z0}.

Fig. 10. The dependence of growth rates of reconnection electric field on the field ratio B_{z0}/B_0 where the open and closed circles show the growth rate for the slow phase γ_1 and that for the fast phase γ_2, respectively. The maximum $\mathbf{E} \times \mathbf{B}$ drift velocity at the input boundary is illustrated by a dashed line for comparison.

Fig. 11. The dependence of four spatial scales on the field ratio B_{z0}/B_0 where the scales are estimated at the period when the current layer becomes thinnest.

Fig. 12. Figure 12 shows the spatial profiles of the current density along the z-axis (top) and in the (x,y) plane (bottom) at $\omega_{ce}t = 118$ for the case of $B_{z0} = B_0$.

Fig. 13. Temporal evolutions of the average velocity along the z-axis for about six thousands marked electrons for five different values of B_{z0} where marked electrons pass across the vicinity of the reconnection point when the reconnection electric field reaches its maximum value.

26

Fig. 14. The temporal evolution of the effective resistivity for five different values of B_{z0} where the resistivity is normalized by the Hall resistivity B_0/qcn_e.

Figure 1

Current Density $-j_z$
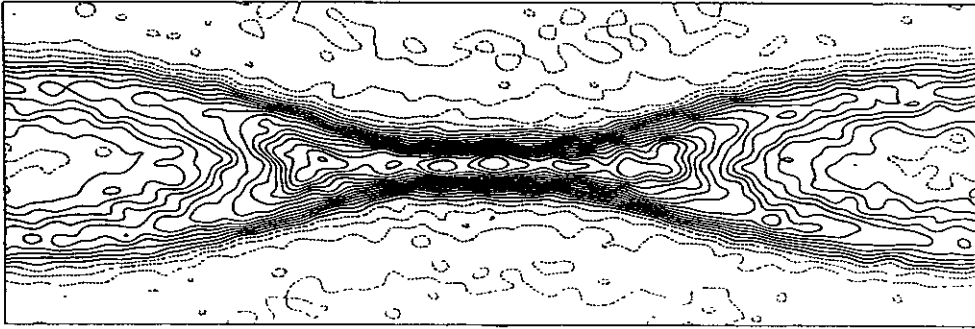
Vector Potential A_z
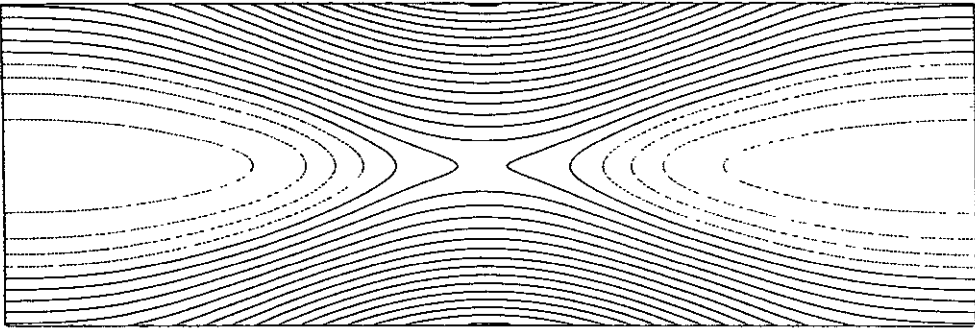
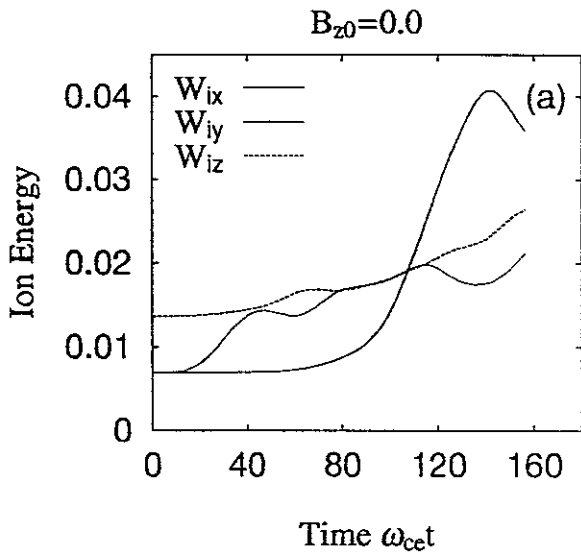## Average Ion Velocity
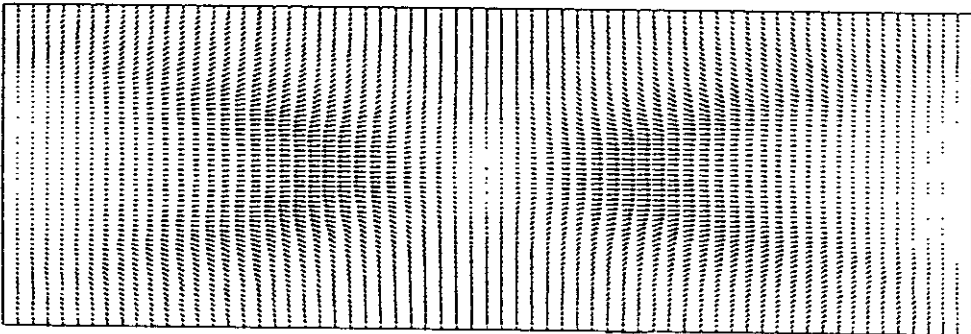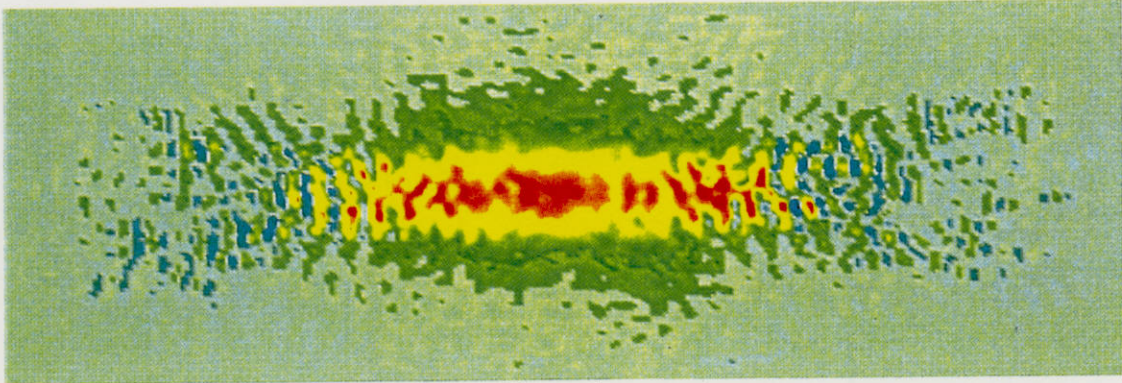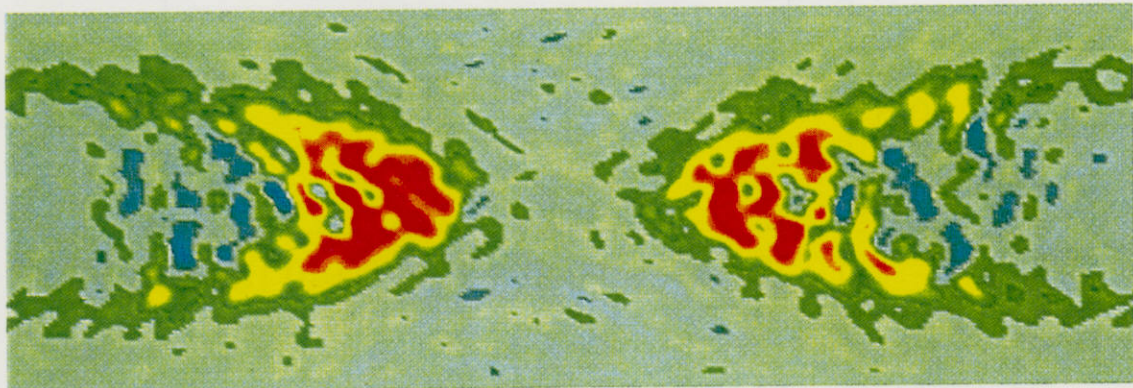

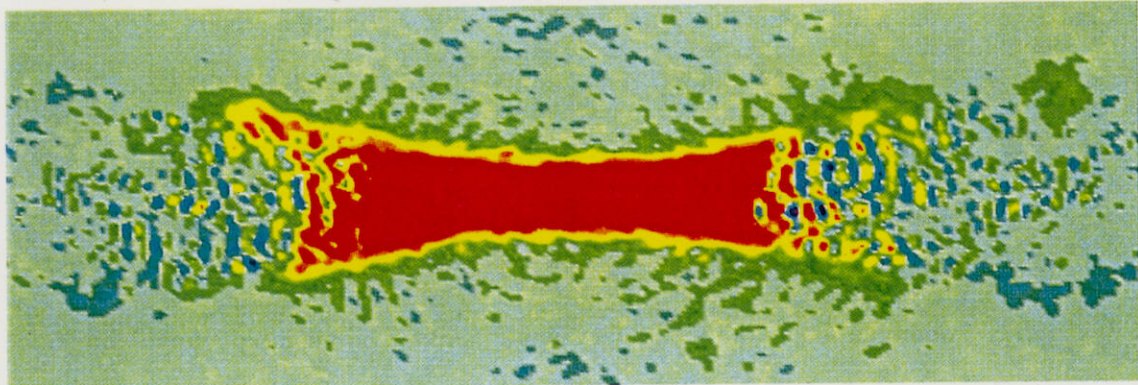## Average Electron Velocity
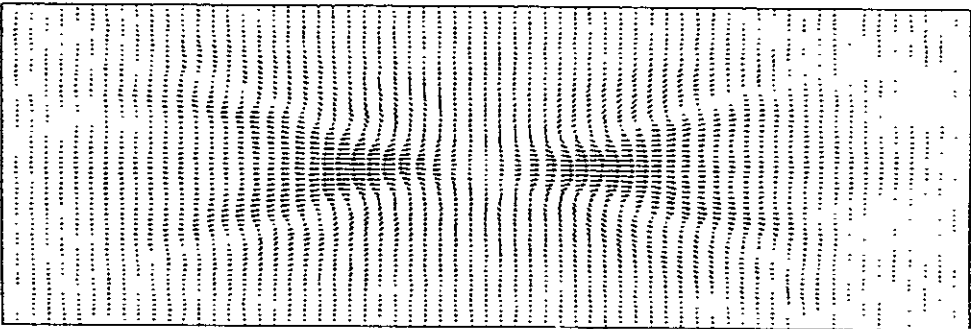
Figure 2
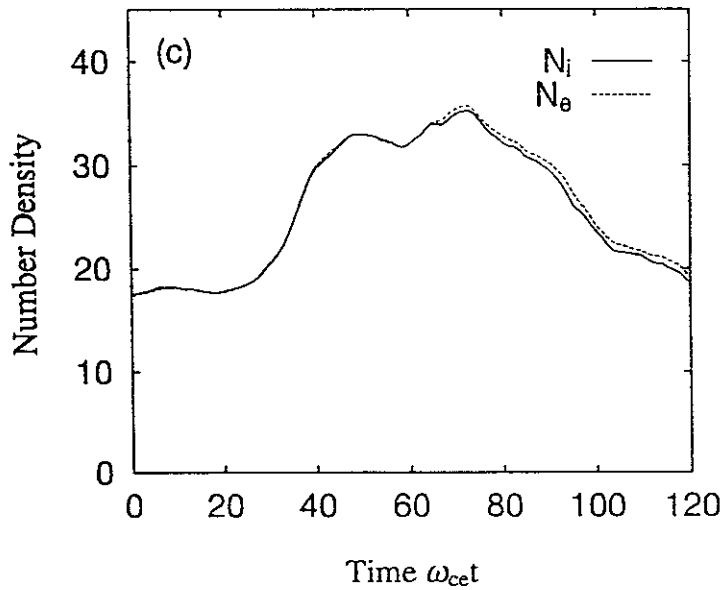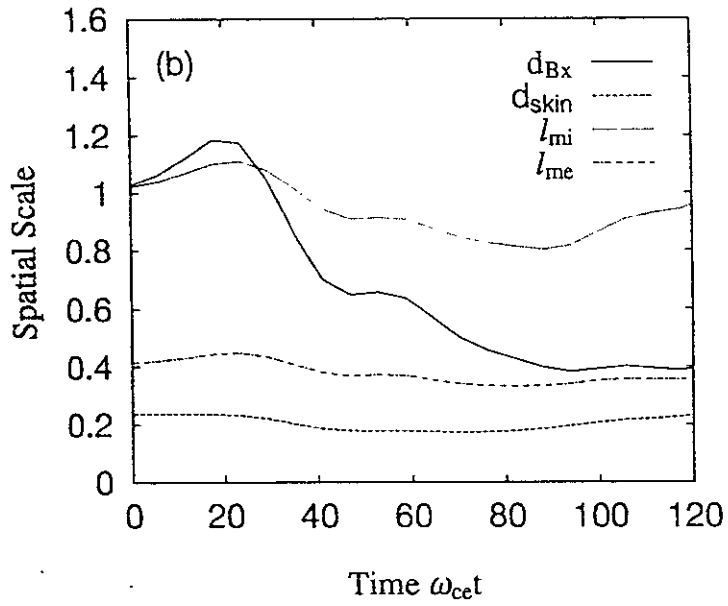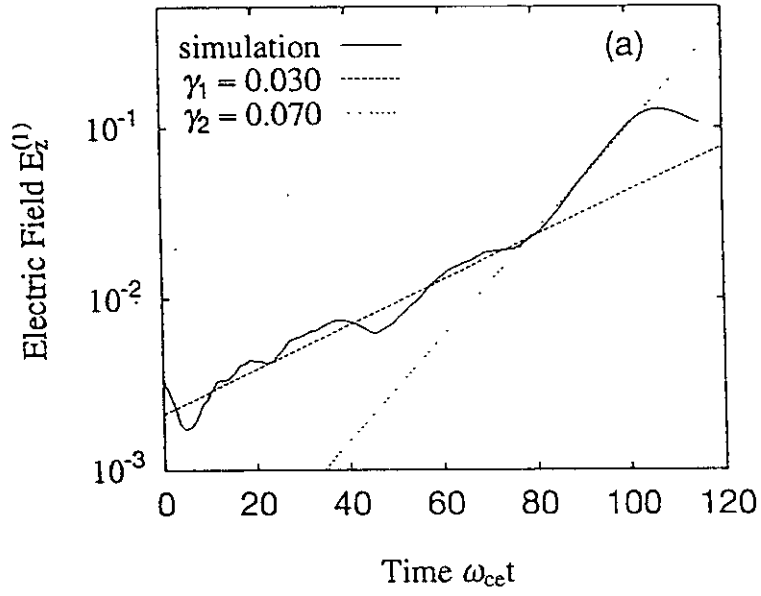
Figure 3
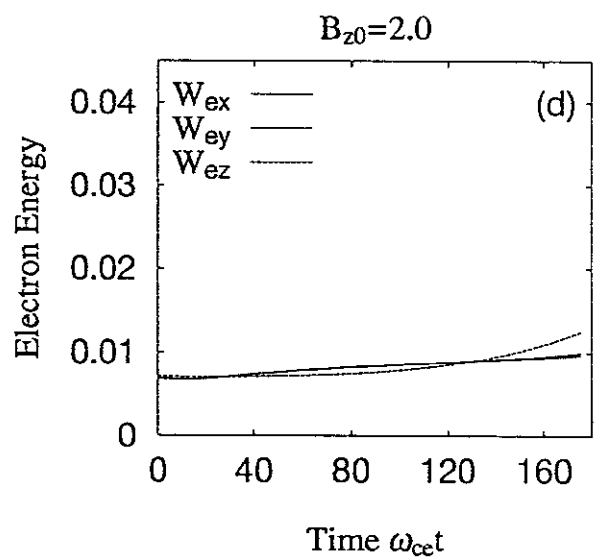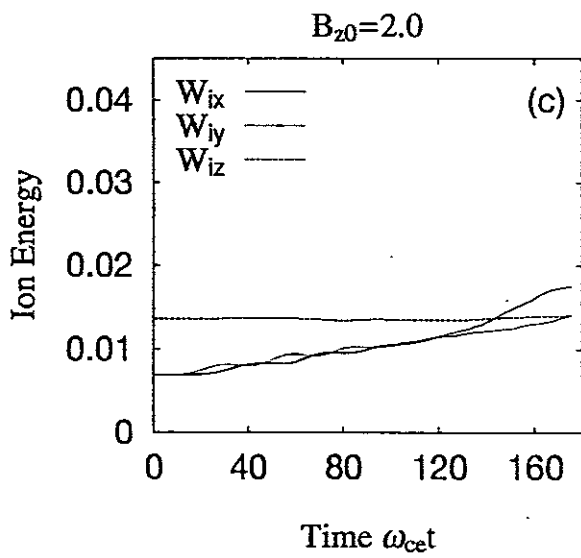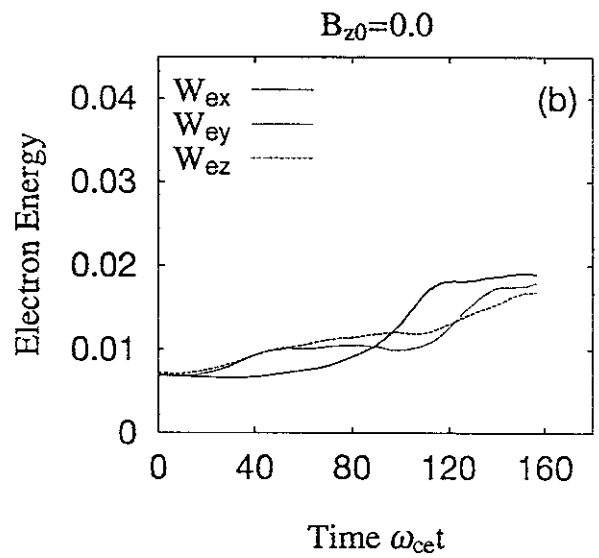
Figure 4

$E_{mg} \cdot j_i$

$E_{st} \cdot j_i$

$E_{mg} \cdot j_e$

$E_{st} \cdot j_e$

Figure 5

$B_{z0}=0.0$

(a)

$E_{st}{\cdot}j_e$
$E_{mg}{\cdot}j_e$
$E_{st}{\cdot}j_i$
$E_{mg}{\cdot}j_i$

Energy Transfer Rate (Arbitrary)

Time $\omega_{ce}t$

(b)

$B_{z0}=0.0$
$B_{z0}=1.0$
$B_{z0}=2.0$
$B_{z0}=3.0$

$E_{mg}{\cdot}j_e$

$E_{st}{\cdot}j_e$

Energy Transfer Rate (Arbitrary)
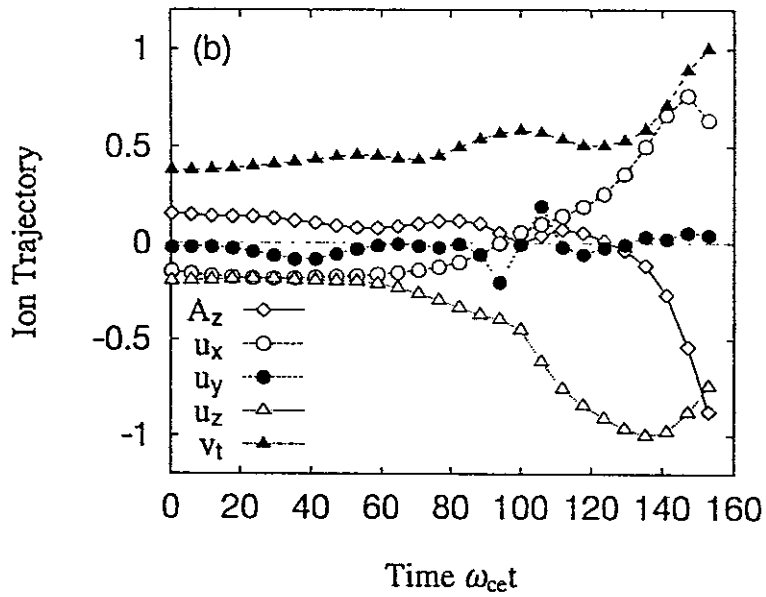
Time $\omega_{ce}t$
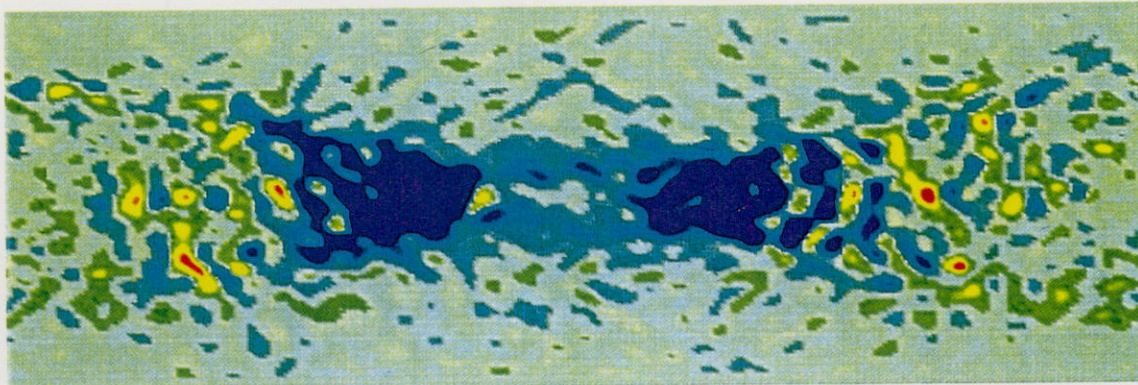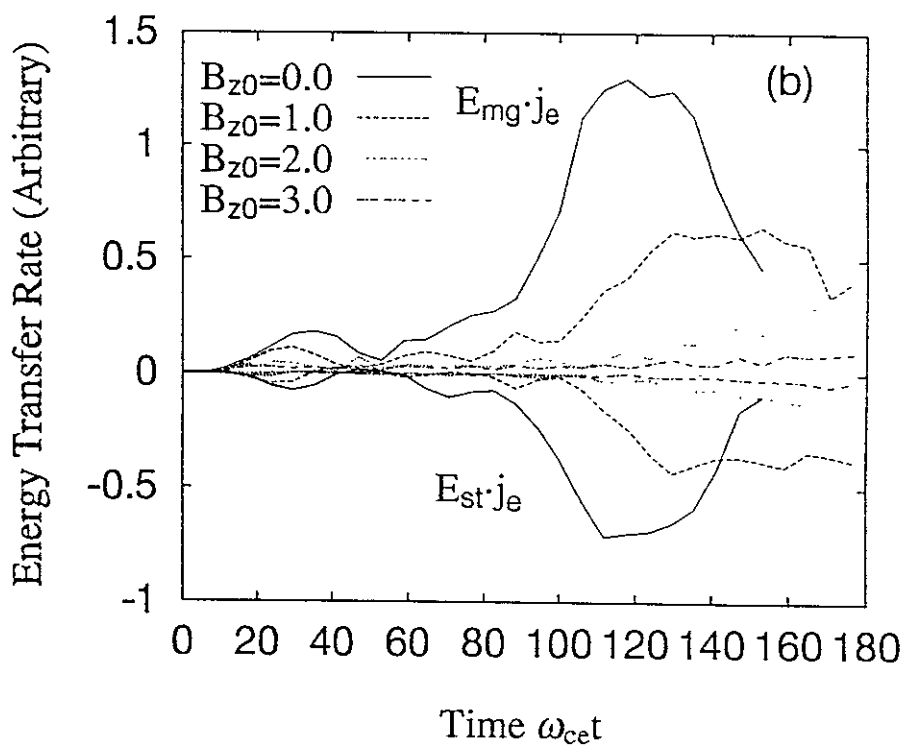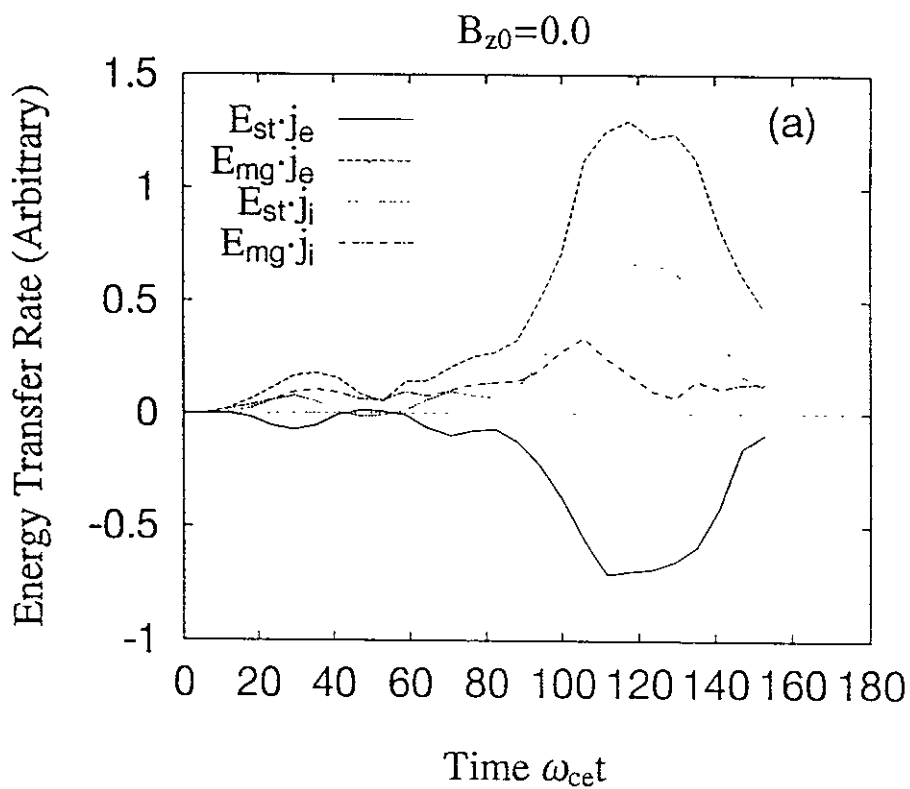
Figure 6

Electron Distribution Function

$f_e(v_z)$

$\omega_{ce}t = 82$

-0.9 v_z 0.9

$f_e(v_z)$

$\omega_{ce}t = 100$

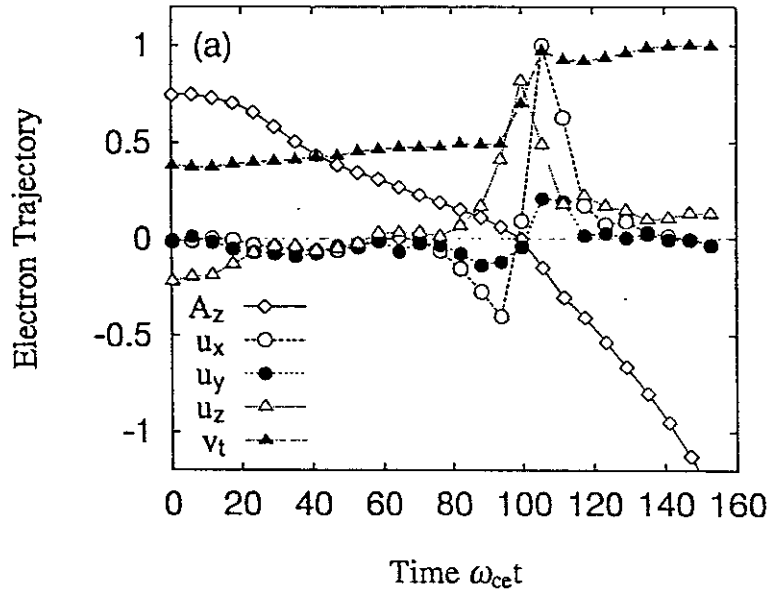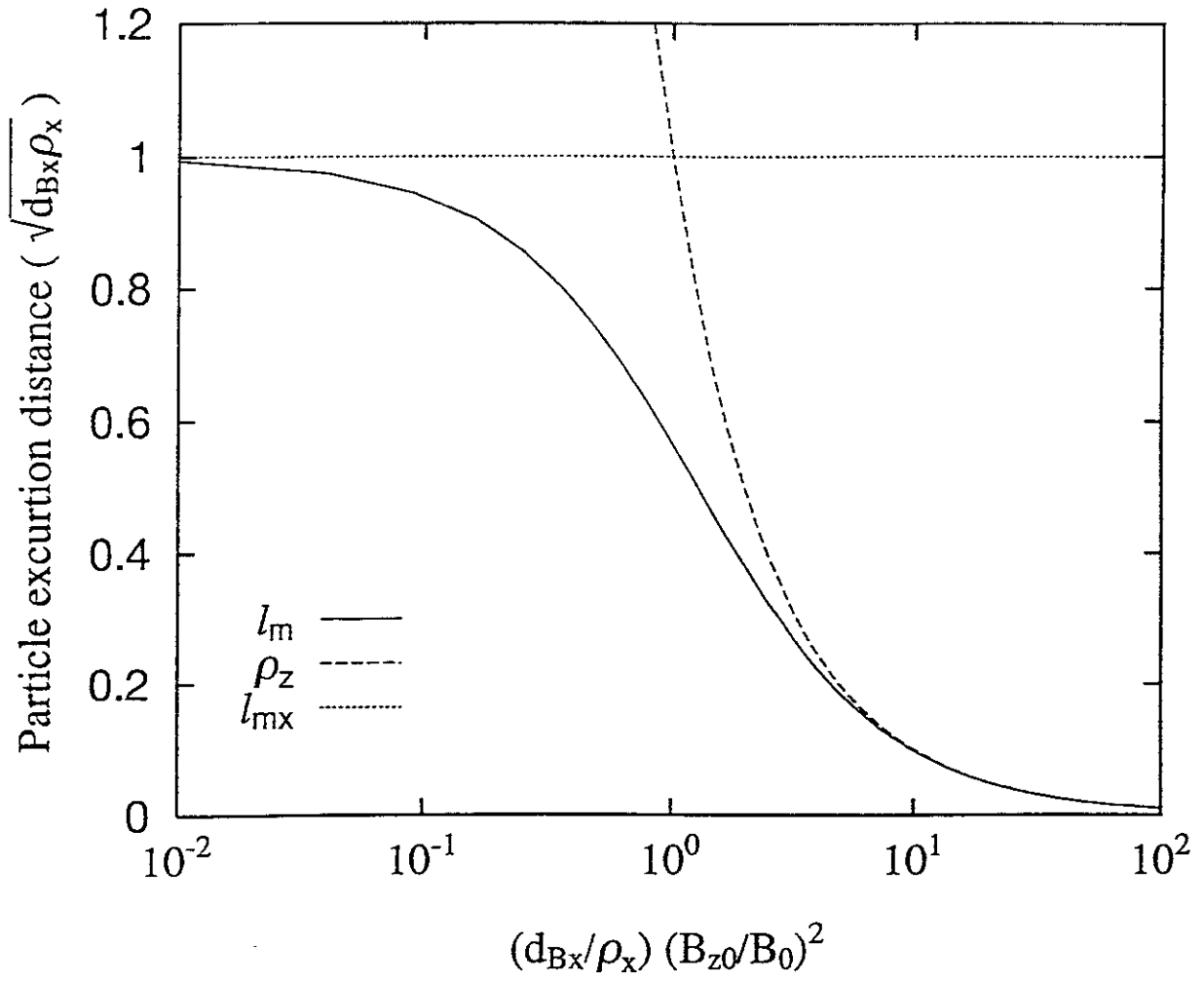-0.9 v_z 0.9

$f_e(v_z)$

$\omega_{ce}t = 118$
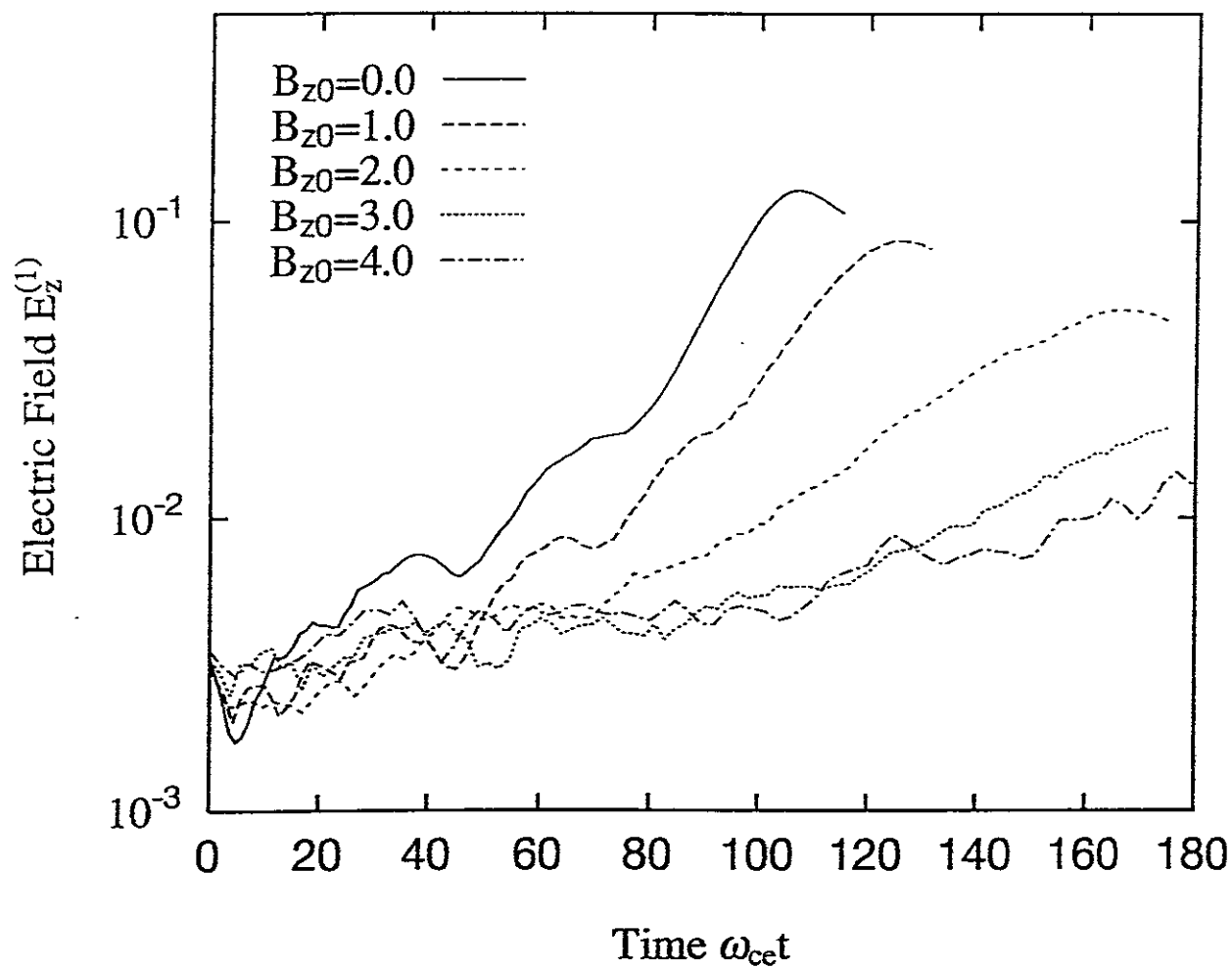
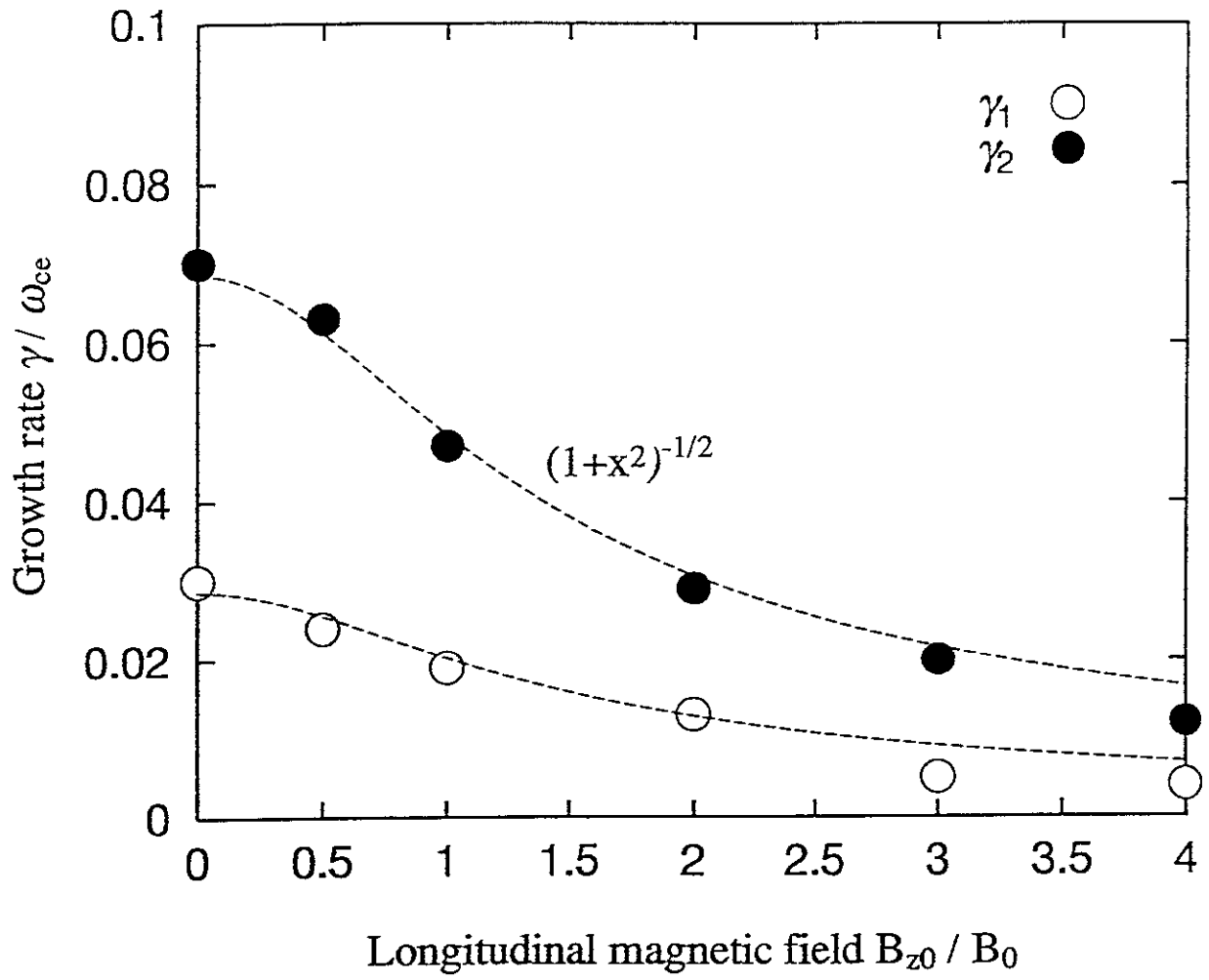-0.9 v_z 0.9
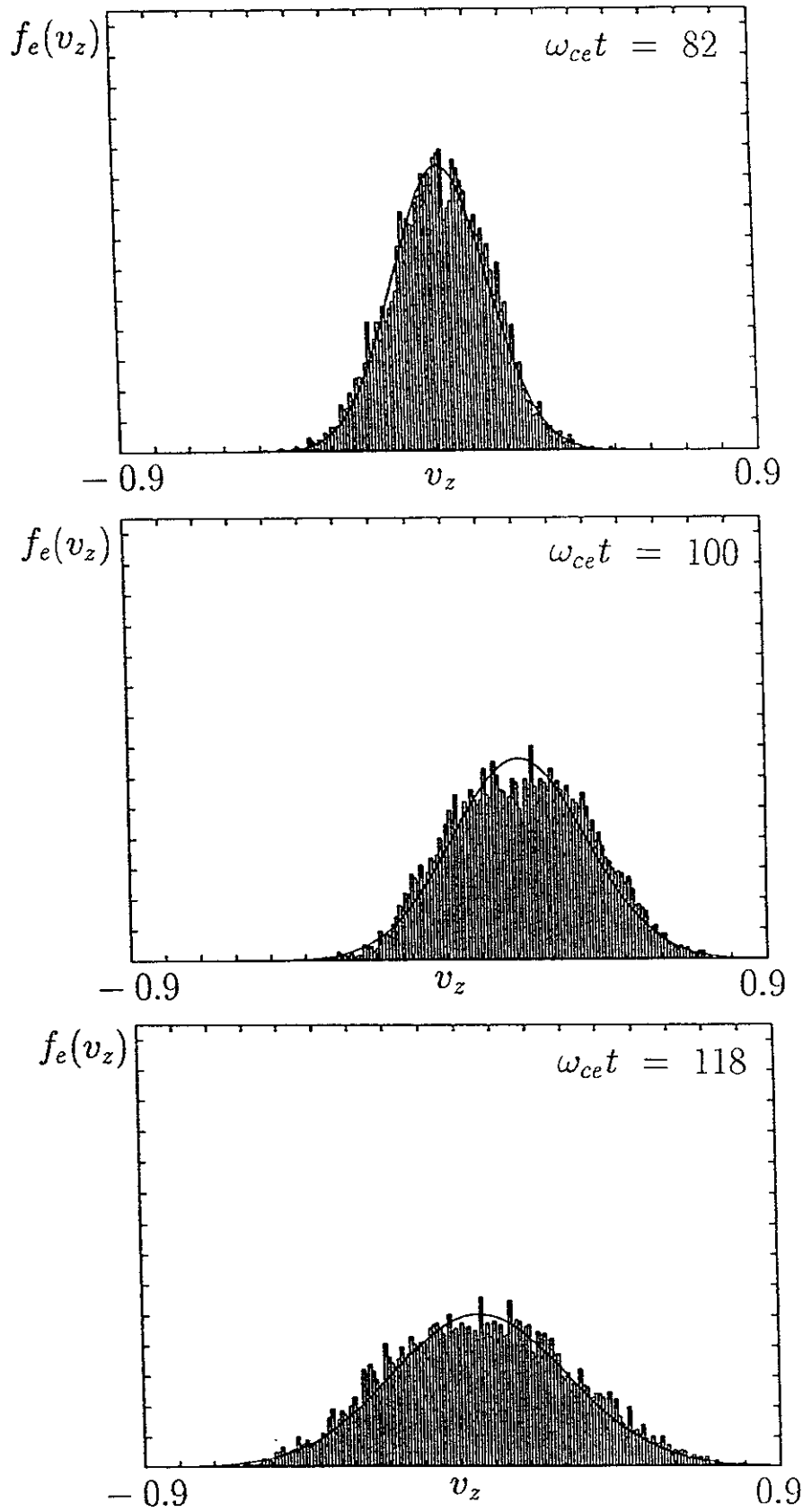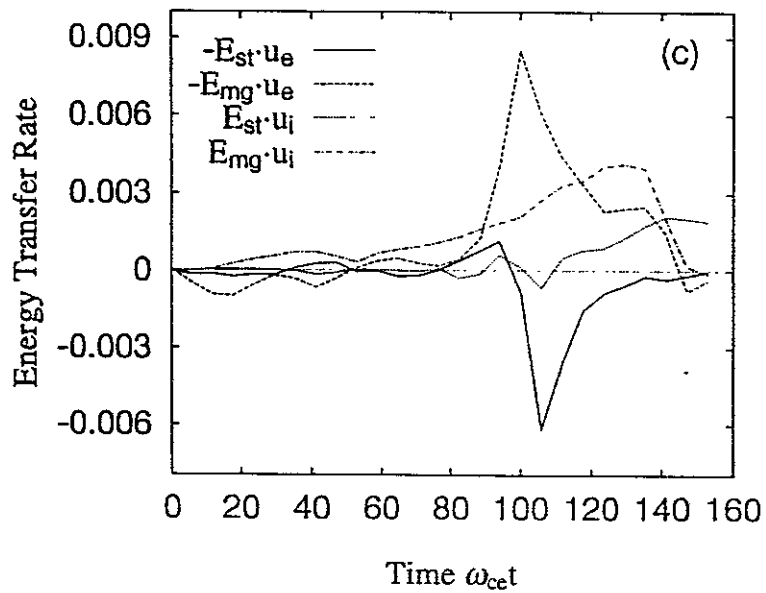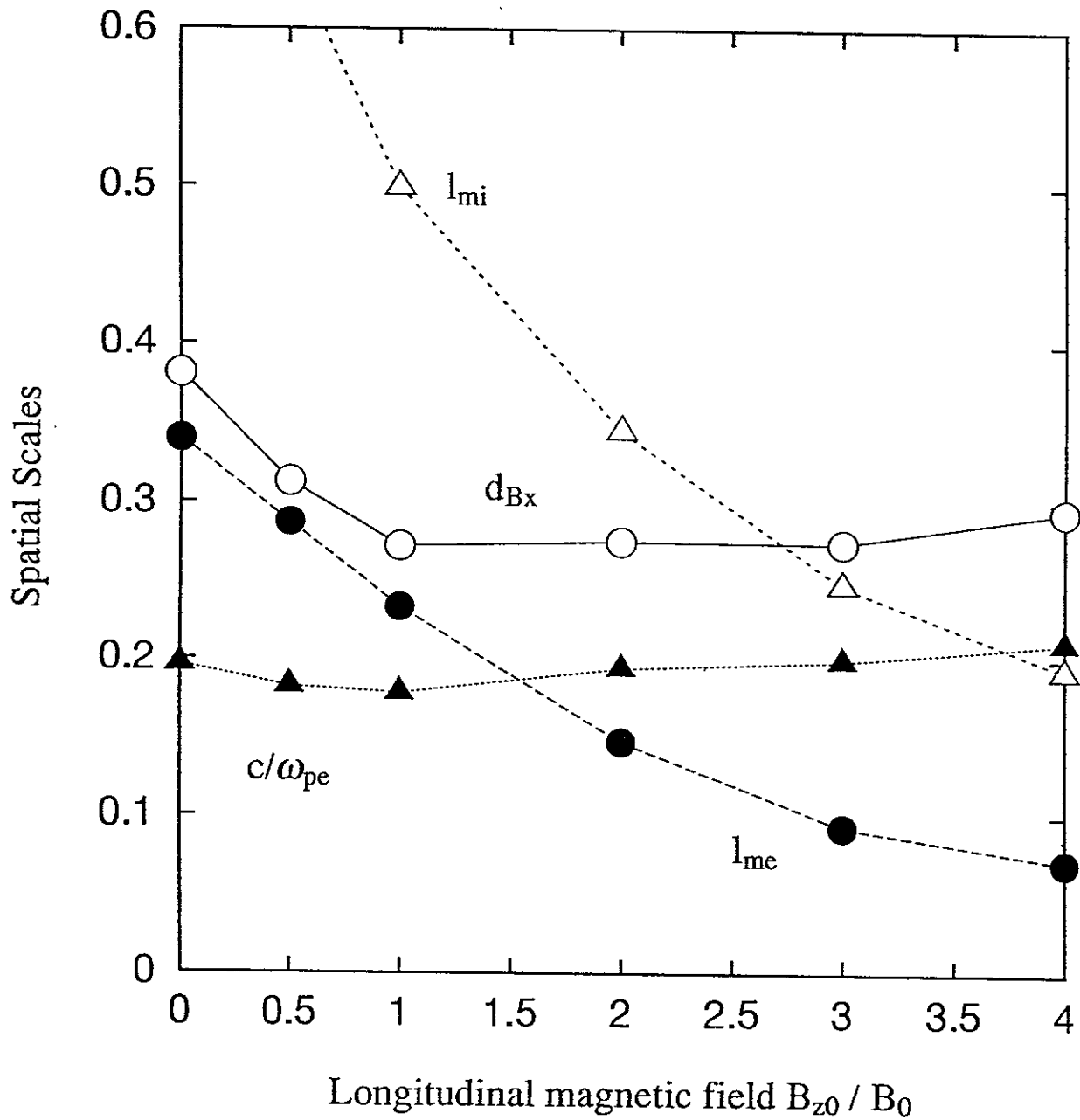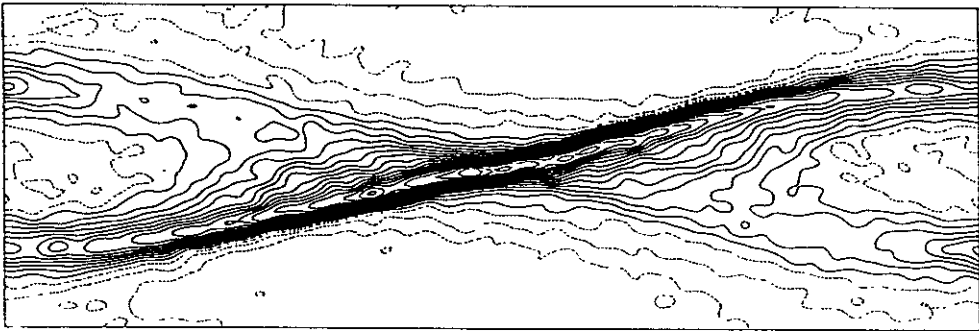
Figure 7

Figure 8

Figure 9

Figure 10

Figure 11

Figure 12

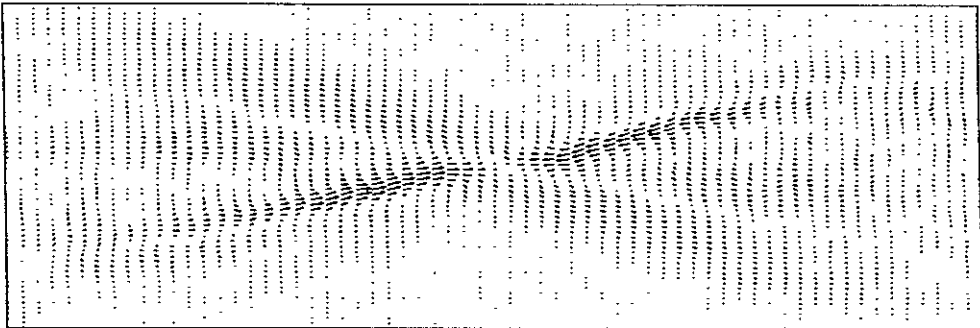Current Density $-j_z$

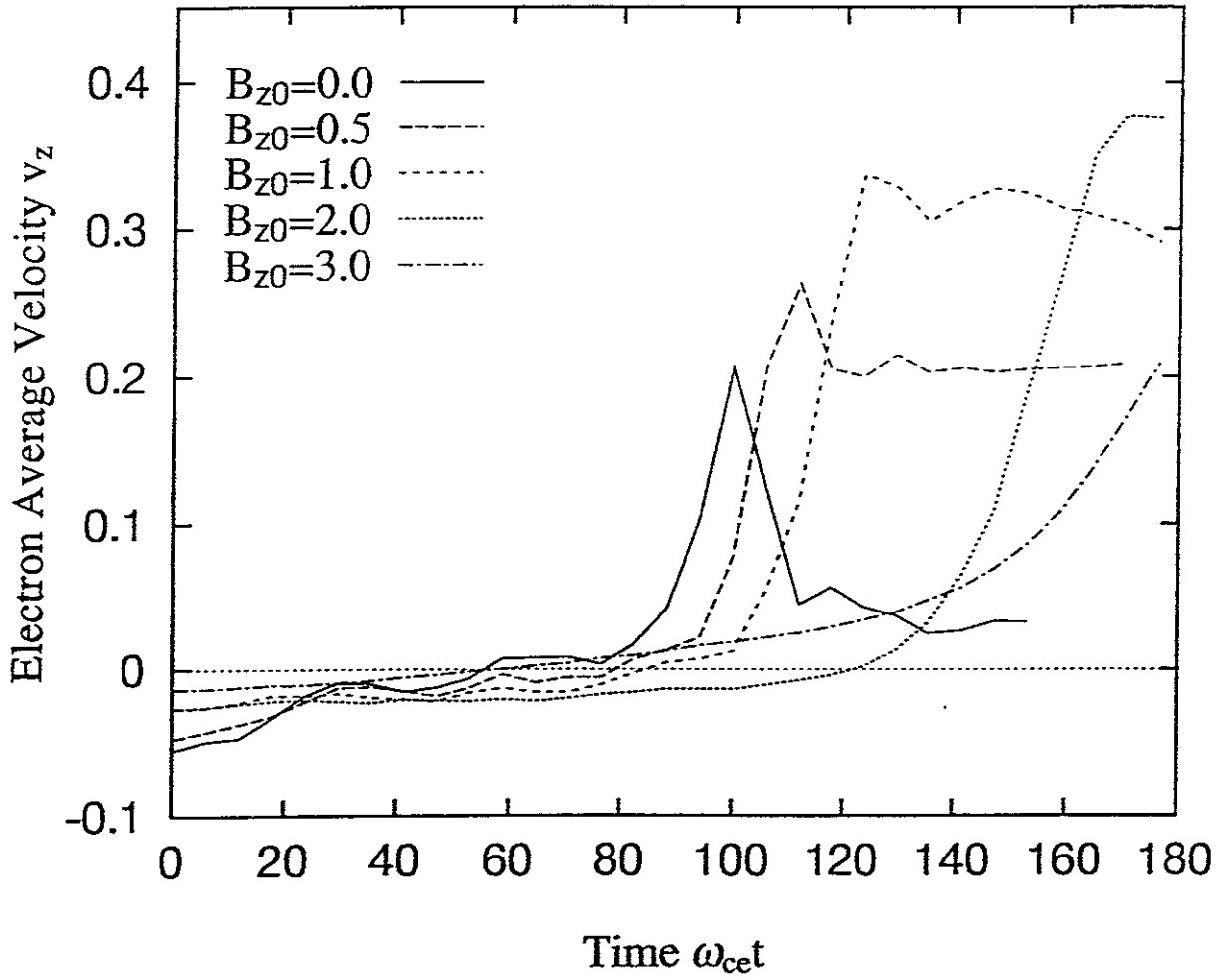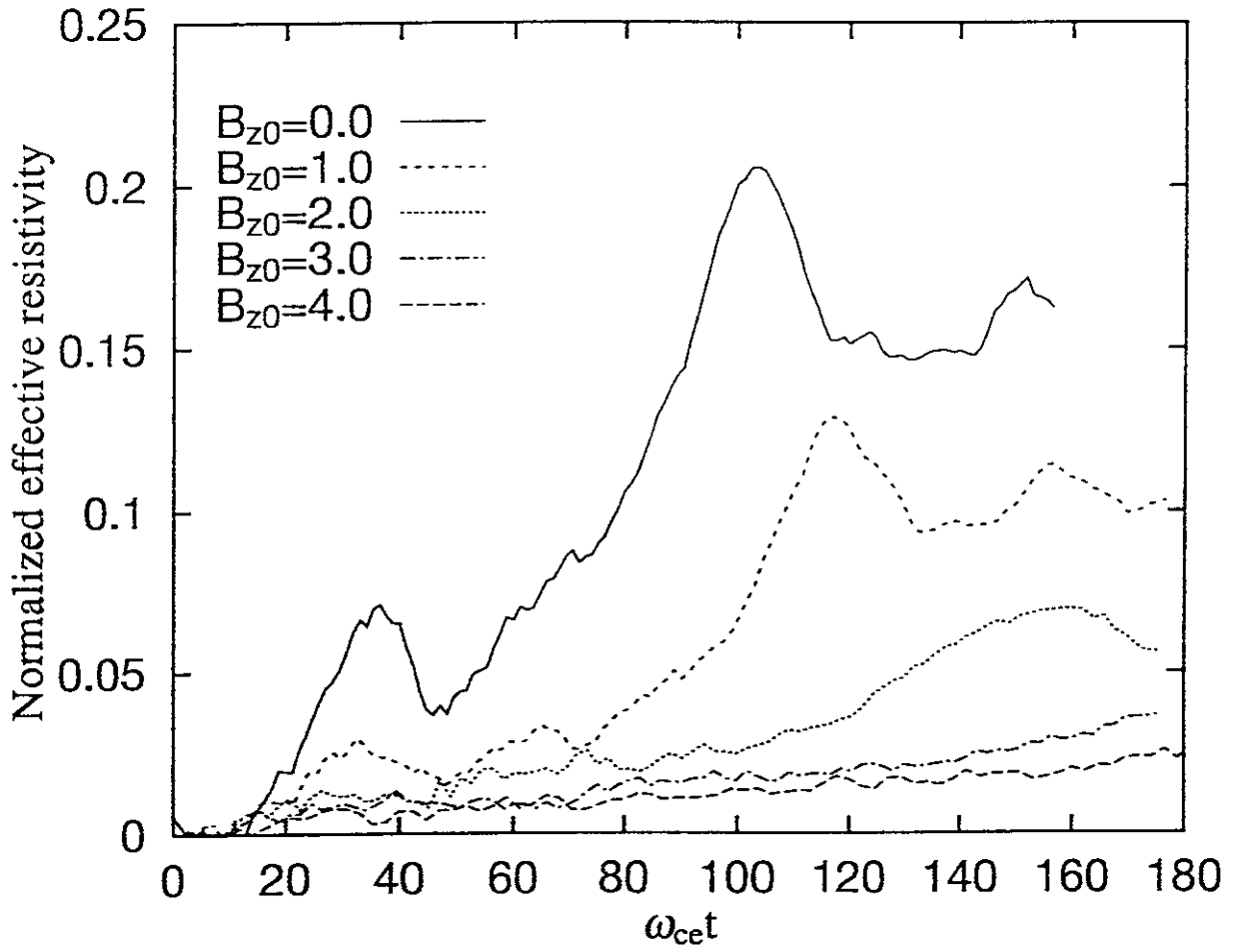Current Density (j_x, j_y)

Figure 13

Figure 14

Recent Issues of NIFS Series

NIFS-388   V.D. Pustovitov,
Control of Pfirsch-Schlüter Current by External Poloidal Magnetic Field in Conventional Stellarators: Dec. 1995

NIFS-389   K. Akaishi,
On the Outgassing Rate Versus Time Characteristics in the Pump-down of an Unbaked Vacuum System; Dec. 1995

NIFS-390   K.N. Sato, S. Murakami, N. Nakajima, K. Itoh,
Possibility of Simulation Experiments for Fast Particle Physics in Large Helical Device (LHD); Dec. 1995

NIFS-391   W.X.Wang, M. Okamoto, N. Nakajima, S. Murakami and N. Ohyabu,
A Monte Carlo Simulation Model for the Steady-State Plasma in the Scrape-off Layer; Dec. 1995

NIFS-392   Shao-ping Zhu, R. Horiuchi, T. Sato and The Complexity Simulation Group,
Self-organization Process of a Magnetohydrodynamic Plasma in the Presence of Thermal Conduction; Dec. 1995

NIFS-393   M. Ozaki, T. Sato, R. Horiuchi and the Complexity Simulation Group
Electromagnetic Instability and Anomalous Resistivity in a Magnetic Neutral Sheet; Dec. 1995

NIFS-394   K. Itoh, S.-I Itoh, M. Yagi and A. Fukuyama,
Subcritical Excitation of Plasma Turbulence; Jan. 1996

NIFS-395   H. Sugama and M. Okamoto, W. Horton and M. Wakatani,
Transport Processes and Entropy Production in Toroidal Plasmas with Gyrokinetic Eletromagnetic Turbulence; Jan. 1996

NIFS-396   T. Kato, T. Fujiwara and Y. Hanaoka,
X-ray Spectral Analysis of Yohkoh BCS Data on Sep. 6 1992 Flares - Blue Shift Component and Ion Abundances -; Feb. 1996

NIFS-397   H. Kuramoto, N. Hiraki, S. Moriyama, K. Toi, K. Sato, K. Narihara, A. Ejiri, T. Seki and JIPP T-IIU Group,
Measurement of the Poloidal Magnetic Field Profile with High Time Resolution Zeeman Polarimeter in the JIPP T-IIU Tokamak; Feb. 1996

NIFS-398   J.F. Wang, T. Amano, Y. Ogawa, N. Inoue,
Simulation of Burning Plasma Dynamics in ITER; Feb. 1996

NIFS-399   K. Itoh, S-I. Itoh, A. Fukuyama and M. Yagi,
Theory of Self-Sustained Turbulence in Confined Plasmas; Feb. 1996

NIFS-400   J. Uramoto,
            A Detection Method of Negative Pionlike Particles from a H2 Gas Descharge Plasma; Feb. 1996

NIFS-401   K.Ida, J.Xu, K.N.Sato, H.Sakakita and JIPP TII-U group,
            Fast Charge Exchange Spectroscopy Using a Fabry-Perot Spectrometer in the JIPP TII-U Tokamak; Feb. 1996

NIFS-402   T. Amano,
            Passive Shut-Down of ITER Plasma by Be Evaporation; Feb. 1996

NIFS-403   K. Orito,
            A New Variable Transformation Technique for the Nonlinear Drift Vortex; Feb. 1996

NIFS-404   T. Oike, K. Kitachi, S. Ohdachi, K. Toi, S. Sakakibara, S. Morita, T. Morisaki, H. Suzuki, S. Okamura, K. Matsuoka and CHS group; *Measurement of Magnetic Field Fluctuations near Plasma Edge with Movable Magnetic Probe Array in the CHS Heliotron/Torsatron;* Mar. 1996

NIFS-405   S.K. Guharay, K. Tsumori, M. Hamabe, Y. Takeiri, O. Kaneko, T. Kuroda,
            Simple Emittance Measurement of H- Beams from a Large Plasma Source; Mar. 1996

NIFS-406   M. Tanaka and D. Biskamp,
            Symmetry-Breaking due to Parallel Electron Motion and Resultant Scaling in Collisionless Magnetic Reconnection; Mar. 1996

NIFS-407   K. Kitachi, T. Oike, S. Ohdachi, K. Toi, R. Akiyama, A. Ejiri, Y. Hamada, H.Kuramoto, K. Narihara, T. Seki and JIPP T-IIU Group,
            Measurement of Magnetic Field Fluctuations within Last Closed Flux Surface with Movable Magnetic Probe Array in the JIPP T-IIU Tokamak; Mar. 1996

NIFS-408   K. Hirose, S. Saito and Yoshi.H. Ichikawa
            Structure of Period-2 Step-1 Accelerator Island in Area Preserving Maps; Mar. 1996

NIFS-409   G.Y.Yu, M. Okamoto, H. Sanuki, T. Amano,
            Effect of Plasma Inertia on Vertical Displacement Instability in Tokamaks; Mar. 1996

NIFS-410   T. Yamagishi,
            Solution of Initial Value Problem of Gyro-Kinetic Equation; Mar. 1996

NIFS-411   K. Ida and N. Nakajima,
            Comparison of Parallel Viscosity with Neoclassical Theory; Apr. 1996

NIFS-412   T. Ohkawa and H. Ohkawa,

Cuspher, A Combined Confinement System; Apr. 1996

NIFS-413   Y. Nomura, Y.H. Ichikawa and A.T. Filippov,
Stochasticity in the Josephson Map; Apr. 1996

NIFS-414   J. Uramoto,
Production Mechanism of Negative Pionlike Particles in H_2 Gas Discharge Plasma; Apr. 1996

NIFS-415   A. Fujisawa, H. Iguchi, S. Lee, T.P. Crowley, Y. Hamada, S. Hidekuma, M. Kojima,
Active Trajectory Control for a Heavy Ion Beam Probe on the Compact Helical System; May 1996

NIFS-416   M. Iwase, K. Ohkubo, S. Kubo and H. Idei
Band Rejection Filter for Measurement of Electron Cyclotron Emission during Electron Cyclotron Heating; May 1996

NIFS-417   T. Yabe, H. Daido,T. Aoki, E. Matsunaga and K. Arisawa,
Anomalous Crater Formation in Pulsed-Laser-Illuminated Aluminum Slab and Debris Distribution; May 1996

NIFS-418   J. Uramoto,
Extraction of K^- Mesonlike Particles from a D_2 Gas Discharge Plasma in Magnetic Field; May 1996

NIFS-419   J. Xu, K. Toi, H. Kuramoto, A. Nishizawa, J. Fujita, A. Ejiri, K. Narihara, T. Seki, H. Sakakita, K. Kawahata, K. Ida, K. Adachi, R. Akiyama, Y. Hamada, S. Hirokura, Y. Kawasumi, M. Kojima, I. Nomura, S. Ohdachi, K.N. Sato
Measurement of Internal Magnetic Field with Motional Stark Polarimetry in Current Ramp-Up Experiments of JIPP T-IIU; June 1996

NIFS-420   Y.N. Nejoh,
Arbitrary Amplitude Ion-acoustic Waves in a Relativistic Electron-beam Plasma System; July 1996

NIFS-421   K. Kondo, K. Ida, C. Christou, V.Yu.Sergeev, K.V.Khlopenkov, S.Sudo, F. Sano, H. Zushi, T. Mizuuchi, S. Besshou, H. Okada, K. Nagasaki, K. Sakamoto, Y. Kurimoto, H. Funaba, T. Hamada, T. Kinoshita, S. Kado, Y. Kanda, T. Okamoto, M. Wakatani and T. Obiki,
Behavior of Pellet Injected Li Ions into Heliotron E Plasmas; July 1996

NIFS-422   Y. Kondoh, M. Yamaguchi and K. Yokozuka,
Simulations of Toroidal Current Drive without External Magnetic Helicity Injection; July 1996

NIFS-423   Joong-San Koog,
Development of an Imaging VUV Monochromator in Normal Incidence

NIFS-424   K. Orito,
            A New Technique Based on the Transformation of Variables for Nonlinear Drift and Rossby Vortices; July 1996

NIFS-425   A. Fujisawa, H. Iguchi, S. Lee, T.P. Crowley, Y. Hamada, H. Sanuki, K. Itoh, S. Kubo, H. Idei, T. Minami, K. Tanaka, K. Ida, S. Nishimura, S. Hidekuma, M. Kojima, C. Takahashi, S. Okamura and K. Matsuoka,
            Direct Observation of Potential Profiles with a 200keV Heavy Ion Beam Probe and Evaluation of Loss Cone Structure in Toroidal Helical Plasmas on the Compact Helical System; July 1996

NIFS-426   H. Kitauchi, K. Araki and S. Kida,
            Flow Structure of Thermal Convection in a Rotating Spherical Shell; July 1996

NIFS-427   S. Kida and S. Goto,
            Lagrangian Direct-interaction Approximation for Homogeneous Isotropic Turbulence; July 1996

NIFS-428   V.Yu. Sergeev, K.V. Khlopenkov, B.V. Kuteev, S. Sudo, K. Kondo, F. Sano, H. Zushi, H. Okada, S. Besshou, T. Mizuuchi, K. Nagasaki, Y. Kurimoto and T. Obiki,
            Recent Experiments on Li Pellet Injection into Heliotron E; Aug. 1996

NIFS-429   N. Noda, V. Philipps and R. Neu,
            A Review of Recent Experiments on W and High Z Materials as Plasma-Facing Components in Magnetic Fusion Devices; Aug. 1996

NIFS-430   R.L. Tobler, A. Nishimura and J. Yamamoto,
            Design-Relevant Mechanical Properties of 316-Type Stainless Steels for Superconducting Magnets; Aug. 1996

NIFS-431   K. Tsuzuki, M. Natsir, N. Inoue, A. Sagara, N. Noda, O. Motojima, T. Mochizuki, T. Hino and T. Yamashina,
            Hydrogen Absorption Begavior into Boron Films by Glow Discharges in Hydrogen and Helium; Aug. 1996

NIFS-432   T.-H. Watanabe, T. Sato and T. Hayashi,
            Magnetohydrodynamic Simulation on Co- and Counter-helicity Merging of Spheromaks and Driven Magnetic Reconnection; Aug. 1996

NIFS-433   R. Horiuchi and T. Sato,
            Particle Simulation Study of Collisionless Driven Reconnection in a Sheared Magnetic Field; Aug. 1996